EXPERIMENTAL AND NUMERICAL INVESTIGATION OF A JET VANE OF THRUST VECTOR CONTROL SYSTEM

A THESIS SUBMITTED TO
THE GRADUATE SCHOOL OF NATURAL AND APPLIED SCIENCES
OF
MIDDLE EAST TECHNICAL UNIVERSITY

BY

BURAK SÖĞÜTCÜ

IN PARTIAL FULFILLMENT OF THE REQUIREMENTS
FOR
THE DEGREE OF MASTER OF SCIENCE
IN
AEROSPACE ENGINEERING

DECEMBER 2019

Approval of the thesis:

EXPERIMENTAL AND NUMERICAL INVESTIGATION OF A JET VANE OF THRUST VECTOR CONTROL SYSTEM

submitted by **BURAK SÖĞÜTCÜ** in partial fulfillment of the requirements for the degree of **Master of Science in Aerospace Engineering Department, Middle East Technical University** by,

Prof. Dr. Halil Kalıpçılar
Dean, Graduate School of **Natural and Applied Sciences** _____

Prof. Dr. İsmail Hakkı Tuncer
Head of Department, **Aerospace Engineering** _____

Assist. Prof. Dr. Mustafa Perçin
Supervisor, **Aerospace Engineering, METU** _____

Examining Committee Members:

Prof. Dr. İsmail Hakkı Tuncer
Aerospace Engineering, METU _____

Assist. Prof. Dr. Mustafa Perçin
Aerospace Engineering, METU _____

Assoc. Prof. Dr. Utku Kanoğlu
Aerospace Engineering, METU _____

Assoc. Prof. Dr. Nilay Sezer Uzol
Aerospace Engineering, METU _____

Assist. Prof. Dr. Onur Baş
Mechanical Engineering, TEDU _____

Date:

I hereby declare that all information in this document has been obtained and presented in accordance with academic rules and ethical conduct. I also declare that, as required by these rules and conduct, I have fully cited and referenced all material and results that are not original to this work.

Name, Surname: Burak Söğütcü

Signature :

ABSTRACT

EXPERIMENTAL AND NUMERICAL INVESTIGATION OF A JET VANE OF THRUST VECTOR CONTROL SYSTEM

Söğütcü, Burak
M.S., Department of Aerospace Engineering
Supervisor: Assist. Prof. Dr. Mustafa Perçin

December 2019, 80 pages

Thrust vectoring is generally used in tactical missile systems when attitude control with conventional control systems is inadequate. One of the most widely used thrust vectoring method is to employ jet vanes in the divergent section of the rocket motor nozzle to have the desired thrust vectoring. In the present study, the flow over the jet vane of a thrust vector control system is investigated using both numerical and experimental techniques. Three dimensional, unsteady and viscous flow over the jet vane is solved numerically, in which the interaction of high temperature and high speed combustion gas flow with the jet vane located in the exit plane of the solid rocket motor nozzle is examined in detail. In addition, static firing tests of a rocket motor, which contains jet vanes at the nozzle exit plane, are conducted in the static rocket motor stand of TÜBİTAK-SAGE. The thrust and the side forces due to the jet vane are measured for different angles of attack values of jet vanes. The nozzle shock pattern in the presence of the jet vane is also visualized by using the Schlieren technique.

Keywords: jet vane, thrust vector control, solid propellant, solid rocket motor, Schlieren, Computational Fluid Dynamic

ÖZ

İTKİ VEKTOR KONTROL SİSTEMİNİN JET KANADININ SAYISAL VE DENEYSEL ANALİZİ

Söğütcü, Burak
Yüksek Lisans, Havacılık ve Uzay Mühendisliği Bölümü
Tez Yöneticisi: Dr. Ör. Üyesi. Mustafa Perçin

Aralk 2019 , 80 sayfa

İtki vektör kontrolü, genellikle taktik füze sistemlerinde geleneksel kontrol sistemleriyle yönelim kontrolünün yetersiz kaldığı durumlarda kullanılır. Roket motoru çıkış konisinde yer alan jet kanatları, istenilen itki vektörünün elde edilmesi için sıklıkla kullanılan itki yönlendirme yöntemlerinden bir tanesidir. Bu çalışmada, itki vektör kontrol sisteminde yer alan jet kanadının etrafındaki akış, hem sayısal hem de deneysel yöntemler kullanılarak incelenmiştir. Jet kanadı üzerindeki üç boyutlu, kararsız ve viskoz akış, sayısal olarak çözülüp; yüksek sıcaklık ve yüksek hızlı yanma sonu gazı akışının, roket motoru lüle çıkış düzleminde bulunan jet kanadı ile etkileşimi ayrıntılı olarak incelenmiştir. Sayısal incelemelere ek olarak, lüle çıkış düzlemindeki jet kanadı içeren roket motorunun statik ateşleme testleri, TÜBİTAK-SAGE'nin statik roket motoru test rampasında gerçekleştirilmiş, itki kuvveti ve jet kanadından kaynaklanan yanal kuvvetler, jet kanatlarının farklı hücum açısı değerleri için ölçülmüştür. Lüle çıkış ekseninde yer alan jet kanadı ile lüle şok etkileşimleri ve akış alanı, Schlieren tekniği ile detaylı olarak görsellenmiştir.

Anahtar Kelimeler: jet kanadı, itki vektör kontrolü, katı yakıt, katı yakıtlı roket motoru, Schlieren, Hesaplamal Akışkanlar Dinamiği

Dedicated to my family

ACKNOWLEDGMENTS

I would like to express my gratitude to Assoc. Prof. Dr. Mustafa PERÇİN for his guidance, interest and faith in this study. Also, I would like to thank Dr. Mehmet KARACA for his interest and support.

Many thanks to my colleagues in TÜBİTAK-SAGE, especially Sertac CURDANELİ, Bora YAZICI and Caner Ekin KİPER, Cetin Ozan ALANYALIOĞLU and Berksu ERKAL for their support and efforts that aided the preparation of this thesis. And special thanks to Dr. Bülent SÜMER, Chief of Propulsion Systems Division in TÜBİTAK-SAGE for his support and faith on research and development efforts and understanding throughout the development of this thesis and my career.

I would specially like to thank my dear Aycan USLU. I am forever grateful for her patience, sweetness, unfailing support and encouragement during this difficult period. She has always managed to motivate me whenever I felt lost and exhausted.

Finally, I would like to thank my mother Mediha SÖĞÜTCÜ, my father Ali SÖĞÜTCÜ and my brother Murat SÖĞÜTCÜ for their support, encouragement and patience during this period. They have always been supportive and understanding throughout my life and I am grateful to have such a family.

TABLE OF CONTENTS

LIST OF TABLES

TABLES

LIST OF FIGURES

FIGURES

LIST OF ABBREVIATIONS

3D	3 Dimensional
AoA	Angle of Attack
BEM	Ballistic Evaluation Motor
CFD	Computational Fluid Dynamics
JD	Jet Deflector
JV	Jet Vane
MATMS	Multi-Axis Thrust Measurement System
SITVC	Secondary Injection Thrust Vector Control Systems
SPRM	Solid Propellant Rocket Motor
SRM	Solid Rocket Motor
SST	Shear Stress Transport
TVC	Thrust Vector Control

LIST OF SYMBOLS

A	Area
A_e	Nozzle exit area
I_{sp}	Specific impulse
M	Mach Number
M_w	Molecular weight
$\dot{m}$	Mass flow rate
P	Pressure
P_a	Ambient pressure
P_c	Chamber stagnation pressure
P_e	Nozzle exit pressure
R	Specific gas constant
T	Temperature
T_c	Chamber stagnation temperature
$\mathbf{v}$	Velocity vector
v_o	Free stream velocity
v_e	Discharged gas velocity
γ	Ratio of specific heats
ρ	Density

CHAPTER 1

INTRODUCTION

Thrust Vector Control (TVC) systems are used to control the attitude of aircrafts and missiles. Highly maneuverable missile systems require the aerodynamic control systems (wings, winglets) and Thrust Vector Control System together.

All TVC systems work the same way: the directional line of the main thrust vector is deflected so as not to pass through the center of gravity of the vehicle and moment is generated which will maneuver the vehicle around its center of gravity as shown in Figure 1.1.

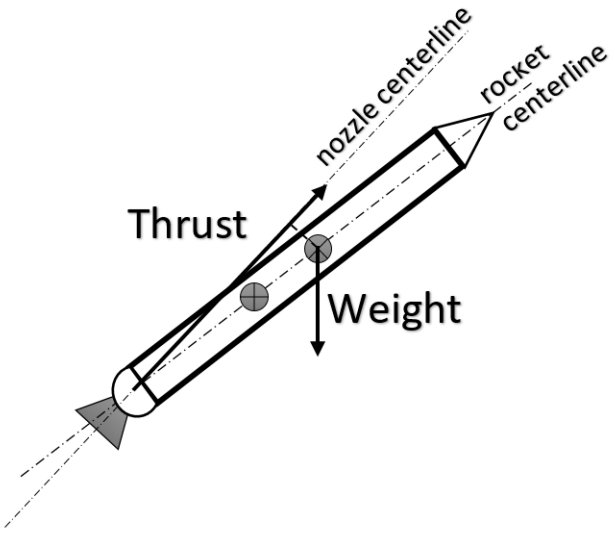

Figure 1.1: Sketch of a thrust vector control system working principle

Deflecting the thrust vector generates pitching, yawing and rolling moments. These moments produce motions such as moving the nose up and down, rolling and turning the missile.

1.1 Thrust Vector Control Systems

Thrust vector control (TVC) systems are generally divided into two main systems as moving and fixed nozzle.

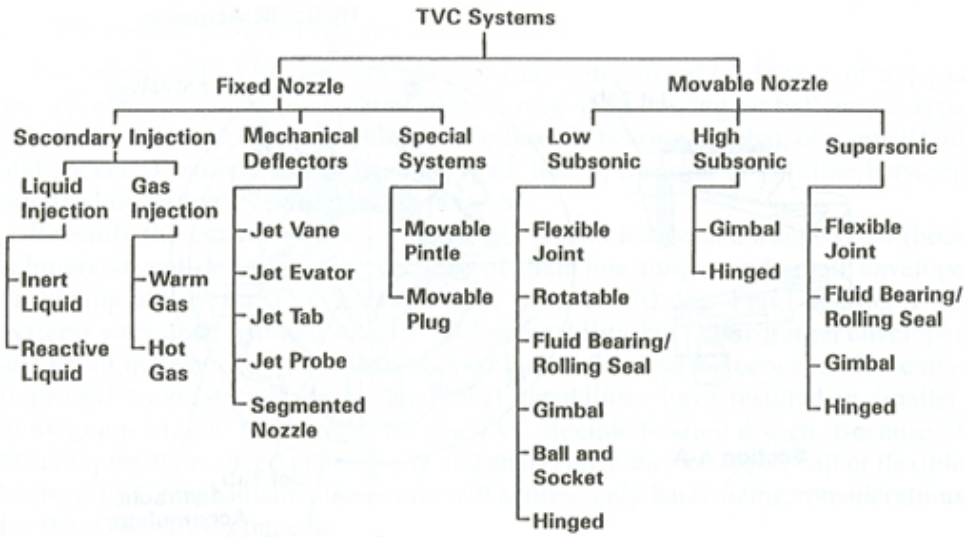

Figure 1.2: TVC systems [1]

TVC systems are divided into different types according to working principles. These are: (1) deflection of burned gases with mechanical guides; (2) rotation of the nozzle; (3) changing the internal pressure distribution of the nozzle. The first one of these principles is provided by the use of a jet vane or a jet deflector, the second one by deflecting the gas out by moving the nozzle with a moving joint, and the third one is provided by the Secondary Fluid Injection (SFI) systems which allow the additional fluids to be injected into the nozzle and to change and direct the pressure distribution within the nozzle [9]. TVC systems will be briefly described in the following sections.

1.1.1 Movable Nozzle Thrust Vector Control Systems

The combustion gas is vectored by the deflection of the nozzle to achieve the desired thrust vector control. Movable nozzle systems are efficient systems. The thrust loss is far less than the other systems because the system produces thrust vectoring by changing the nozzle angle and there is no mechanical deflector or other deflectors in the flow that may cause axial thrust loss [9]. Movable nozzle TVC systems

are divided into three basic types according to the nozzle exit velocity and divided into sub-branches according to the control mechanisms. In Figure 1.3, three basic movement mechanisms are shown.

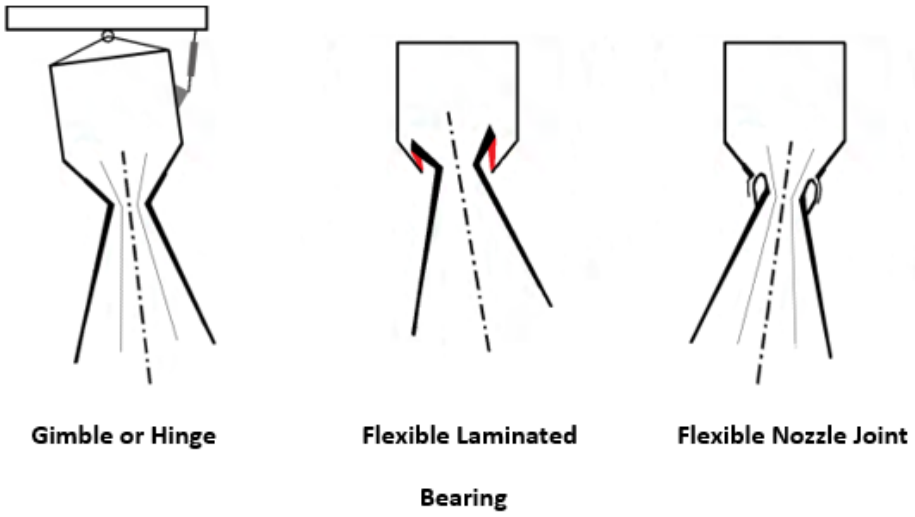

Figure 1.3: Movable nozzle mechanisms

1.1.1.1 Gimbal Type Nozzle

The TVC systems with moving nozzles are classified by small differences. In movable nozzle systems, the divergent part of the nozzle can be rotated independently of the convergent part with different mechanical interfaces. In the movable TVC system, the external geometry is divided into two parts: the throat and the fixed part. The expansion part is the moving part and the diverging part is the fixed part. The outer geometry of the moving part is rounded and integrated like a hinge so that it can rotate about the fixed part Figure 1.4. In this TVC system, sealing is the greatest problem in the rounded part where the nozzle throat inserted into the mechanically fixed section [9].

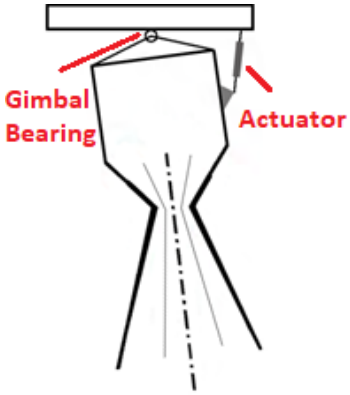

Figure 1.4: Gimbal type nozzle

1.1.1.2 Flexible Nozzle Joint

Flexible articulated TVC systems are used today in large strategic and satellite launching systems as well as in tactical systems requiring $5 - 15°$ vector angle [9]. Flexible nozzle joints have a layered structure formed by bonding elastomer and reinforcing layers to each other and to the front and back rings (Figure 1.5) [2]. Orientation is achieved through shear deformation of the elastomeric layers. The reinforcing layers are made of metal (steel) or composites. The elastomers which are used so far are silicon, natural rubber and synthetic polyisoprenes. Flexible joint systems can be used in a wide range of temperatures, making them suitable for submerged nozzle systems. Flexible joint torque values increase with increasing vector angle, pressure and aging [10].

The general application is spherical, but there are conical applications [2]. When deflected at a certain angle in any direction, the elastomer layers are subjected to shear deformation and stiffness of the layers rotated by a certain ratio of the total vector angle [11]. Flexible nozzle joint design involves the selection of joint configuration, the number of reinforcement elements and the choice of material, elastomer and environmental factors.

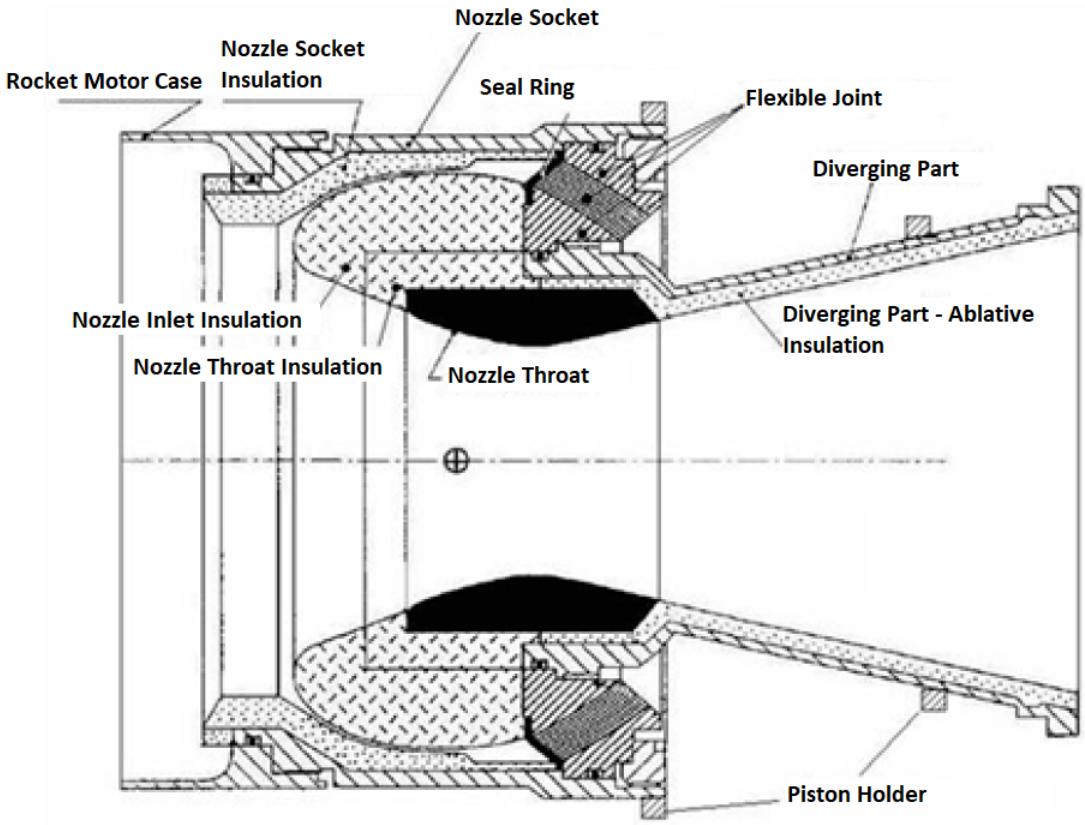

Figure 1.5: Flexible nozzle parts [2]

1.1.2 Secondary Injection Thrust Vector Control Systems(SITVC)

Secondary injection TVC systems operate with the principle that the flow of propellant gases in a fixed nozzle directed by another secondary hot or cold gas that is injected in (Figure 1.6). Secondary injection diverts the gas flow in the nozzle by perturbing the supersonic flow to create an oblique shock wave. An impulse vector is provided by the torque generated.

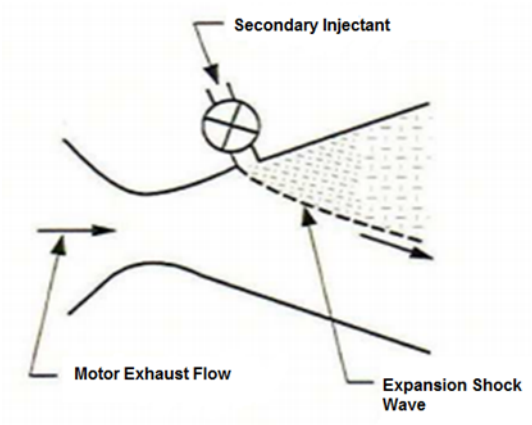

Figure 1.6: Basic flow structure with SITVC [3]

A secondary gas is injected at diverging part of the converging-diverging nozzle where the flow is supersonic. The pressure distribution in the nozzle is used to direct the side forces acting on the air vehicle as a result of the disturbed flow [3].

The systems using SITVC are generally seen in large and heavy systems. The main reason why this method cannot be applied to small systems is the volume required for the additional equipment (secondary fluid reservoir, pump, etc.) needed by the SITVC system. However, the SITVC system does not require any moving parts and a mechanical obstacle to create a thrust vector as a gimbaled nozzle or a jet vane. [9]

1.1.3 Fixed Nozzle Thrust Vector Control Systems

In these systems, thrust vector control is provided by deflecting the rocket motor exhaust gases using mechanical obstacles. Such systems use a jet vane or a jet deflector, which mechanically changes the direction of flow at the nozzle exit area (Figure 1.7). Jet vanes change the direction of flow by small wings placed on the inner surface of the nozzle. On the other hand, jet deflector systems provide rotational torque on the rocket by controlling the gas output with the aid of deflectors moving in the plane of the nozzle outlet.

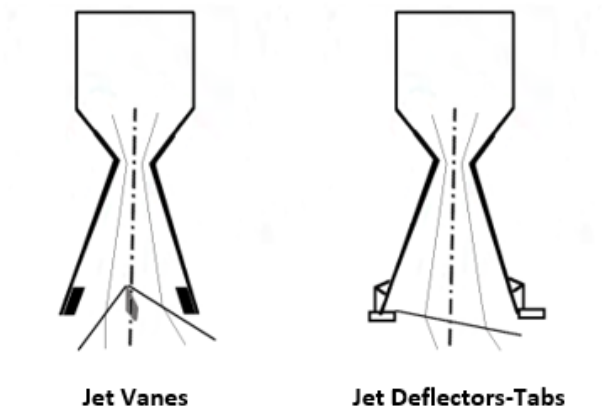

Figure 1.7: Jet vanes and jet deflectors-tabs sketch

In the fixed nozzle TVC systems, the vector control basically provides a mechanical obstacle at the nozzle exit, deflecting the flow. This obstacle for the thrust vector control causes the loss of axial thrust in fixed nozzle systems more than that of moving nozzles [9].

The jet vane (JV) / jet deflector (JD) system is determined to be useful in relatively light and small systems, which require higher maneuverability. These systems are used in a wide range of applications.

1.1.3.1 Jet Deflector / Jet Tab / Jetavator TVC Systems

In these systems, mechanical deflectors are located around the exit area of the nozzle and the propulsion vector control is provided by this deflector located at the exit of the nozzle (Figure 1.8 and 1.9). These systems do not create a rolling moment on the missile while generating yawing and pitching moments. Jet deflectors and jet tabs are blunt structures created with the aim of preventing the flow at the exit of the nozzle. For this reason, the use of jet deflector and jet vane cause excess power loss. Placing the JD at the end of the nozzle causes the shock wave to occur before the deflector and the pressure on the deflector increase. The resulting pressure increase also creates a side force. This side force is directly proportional to the values of the JD area and the nozzle exit area. The side force is adjusted by moving the JD at the nozzle outlet

enlarging and reducing the nozzle outlet area.

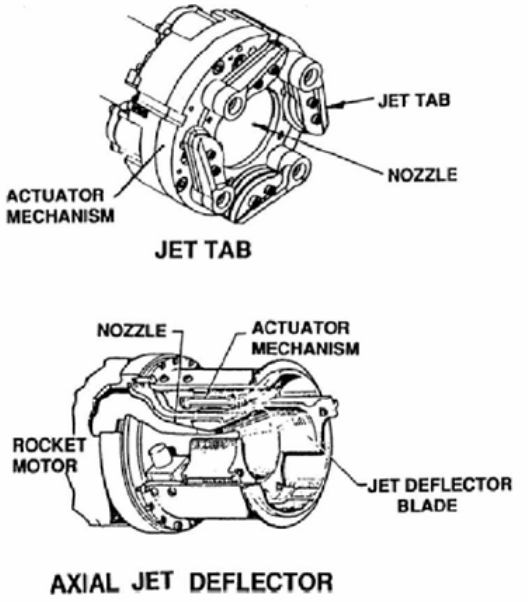

Figure 1.8: Jet vanes and jet deflectors-tabs [4]

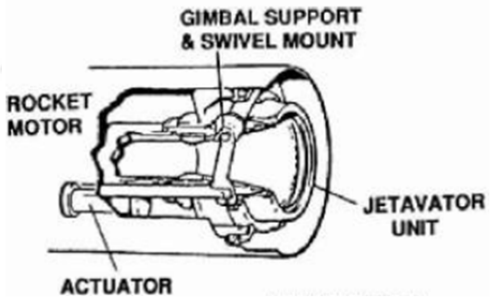

Figure 1.9: A sketch of a jetavator [4]

1.1.3.2 Jet Vane TVC Systems

In jet vane TVC systems, a vane is placed at the exit of the nozzle and the vane base follows the contour of the nozzle. The jet creates yawing and pitching moments in addition to rolling moment with respect to the missile centerline. The jet vane control was first used in German V-2 missile [9].

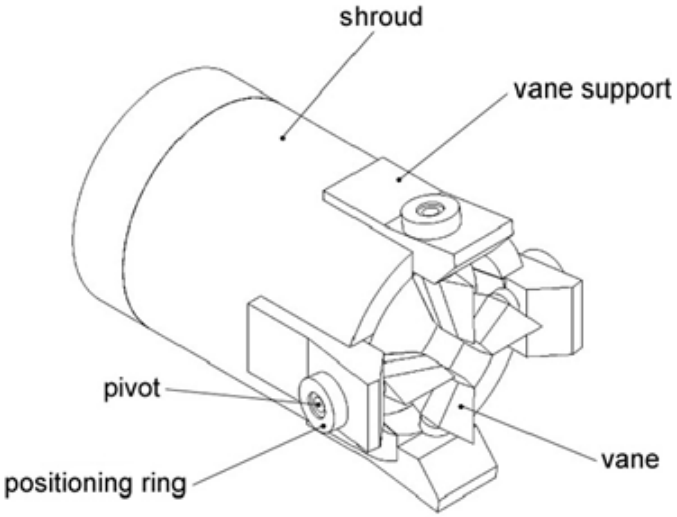

Figure 1.10: JVTVC system mounted at the exit from the nozzle assembly [5]

Jet Vane TVC systems are one of the effective TVC systems that are used in missiles. The vane is characterized by any small fin or plate that is directly placed in the exiting flow of the nozzle to control the thrust vector (Figure 1.10). The principle of generating control forces using jet vanes is similar to producing lift with a supersonic wing at an angle of attack in a supersonic flow. The pressure difference between the upward and downward sides of the jet vane provides a force normal to the chord of the jet vane. The normal force has a component in the lift direction, also referred to as side force, and it is useful to control the missile. However, the generation of the useful lift is accompanied by drag, which results in a loss in the thrust force generated by the propulsion system. The main objective of the design of a jet vane is to generate side force with minimum drag. The advantages and disadvantages of the aforementioned systems are summarized in Table 1.1.

Table 1.1: TVC systems comparison

TVC System	Advantage	Disadvantage
Flexible Joint	• Improved characterization and application level, high reliability • Wide operating temperature range • High sealing performance • Negligible "Coulomb" friction	• High deflection torque • High volume requirement at vector angles greater than 15° • Sliding rotating point • Thermal protection requirement • Complex and large control-drive system
The ball-and-socket	• Improved characterization and application level, high reliability • $\pm 20^\circ$ Thrust Vector Angle • Low volume • Small drive system needs	• Constant axial load requirement for sealing • The need for an anti-rotation system to provide axial rotation • High thrust loss • Unpredictable friction coefficient • Leakage problem
Jet vane	• Rotation control • $\pm 10^\circ / \pm 10^\circ$ Thrust Vector angle • Nozzle -free replacement • Low torque requirement • Fast response capacity	• High thrust loss • Limited to low temperature burned gases or rocket motor with short duration of burning • Relatively high weight • High jet vane angle provide small thrust vector angle
Jet deflector/tab	• Low risk / High development • Low volume • Fast response capacity • The horizontal force is directly proportional to the ratio of the deflector area to the nozzle area	• High thrust loss • Limited to low temperature burned gases or rocket motor with short duration of burning • High torque • Relatively high weight
SITVC	• Fast response capacity • The injected secondary gas impulse is added to the motor impulse • Less pre-launch control requirement	• $\pm 6^\circ / \pm 6^\circ$Thrust vector angle (Max) • High weight • Hard to choose suitable fluid

1.2 Solid Propellant Rocket Motor and TVC Systems

1.2.1 Fundamentals of Solid Propellant Rocket Motor

The general meaning of propulsion is to drive a system forward. Propulsion systems change the velocity or the attitude of air vehicles, systems or bodies. Propulsion systems are classified into two categories: (1) system that produces the thrust by ejecting stored material; (2) system that uses the material from the surrounding environment to produce thrust. A rocket propulsion system generates thrust by ejecting the stored and burned highly energetic materials. Ducted propulsion systems include turbojets, turbofans and ramjets which use stored fuel with the environment as a working fluid. These propulsion systems include complex components such as rotating parts and injectors [12].

Some missiles use simple propulsion systems. These kinds of propulsion systems generally have a one-time operating system. The system starts to propel and ends after the motor is burned. These relatively simple systems use a solid propellant rocket motor. The solid propellant rocket motor consists of a cylindrical case with propellant bonded to its inner surface, a hollow combustion chamber and a nozzle to direct the flow of gases out of the chamber. Figure 1.11 shows a schematic of a typical rocket motor.

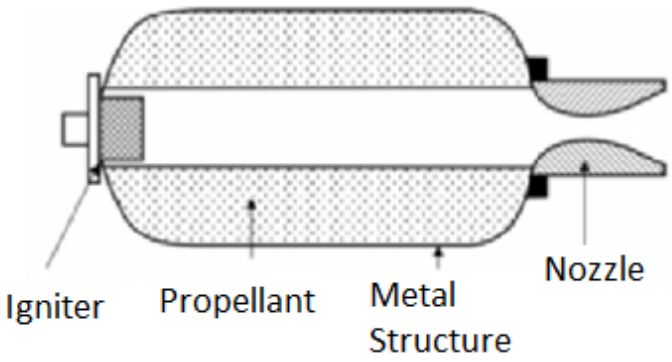

Figure 1.11: Solid rocket motor [6]

The propellant surface, after reaching its melting temperature forms a liquid layer called the foam layer which contains a mass of bubbling gaseous products and molten

propellant. Final combustion gas and metal fuel products are detected in the gas-phase flame region. These products are convected towards the nozzle (Figure 1.12) .

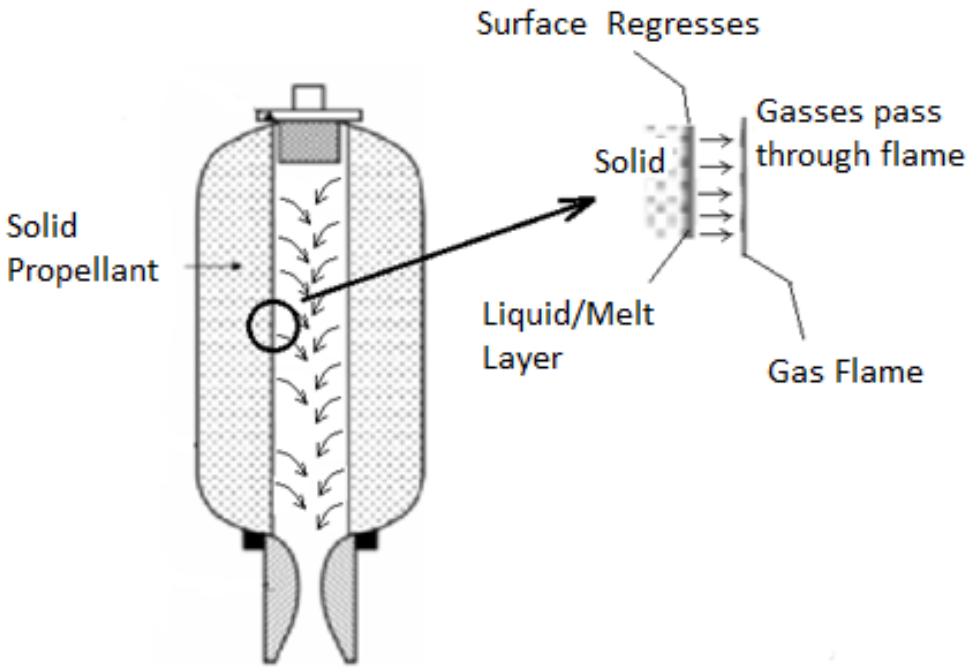

Figure 1.12: Solid rocket motor and surface burning [6]

A simple rocket motor consists of an external body, a convergent-divergent nozzle, a fuel core and an igniter. Solid fuel starts burning from the surface by the trigger provided by the igniter. The produced hot gases increase the pressure swiftly. The rising pressure allows these gases to be pushed out of the nozzle rapidly. The ejected mass provides the impulse needed. However, due to the section of the straight throat, the mass of gas expelled is limited. Therefore, the pressure values of the combustion and the combustion rate of the solid fuel are also limited.

The solid propellant rocket motor systems have a lower specific impulse (Isp) compared to air-breathing propulsion systems, but they are superior to air-breathing propulsion systems in terms of their acceleration capability. In addition, the operation of the solid propellant rocket motors is independent of the Mach number.

1.2.2 Internal Ballistic of SPRM

The requirements characterize the features of the rocket motor. The requirements are achieved by internal ballistic parameters. By considering internal ballistic parameters, rocket motor internal flow solution can be inspected.

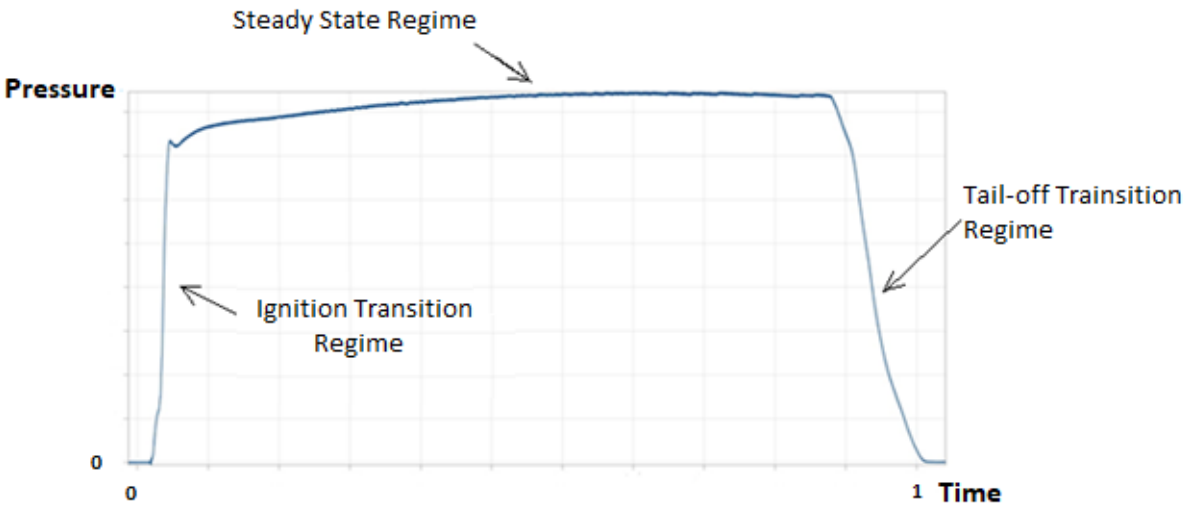

Figure 1.13: Combustion chamber normalized pressure - time curve

Chamber pressure, as shown in Figure 1.13, is the gas pressure inside the combustion chamber during the motor operation. The main constraint in the SRM design is the chamber pressure. Structural components are designed to withstand the maximum chamber pressure.

Thrust is the base design constraint of a propulsion system. The thrust of an SRM is the force generated rocket propulsion system acting on the missile in the flight direction. Thrust (T) is a function of the mass flux, velocity, pressure at the nozzle exit, ambient pressure and nozzle exit area [13]:

$$T = \dot{m}_e v_e + (p_e - p_0) A_e \tag{1.1}$$

1.3 Literature Survey

In order to comprehend the complex flow conditions around jet vanes, many researchers perform experimental and numerical investigations.[9-14]. However, a limited number of studies in the literature report results of static firing tests with force and moment measurements by using SRMs and jet vanes in order to understand the performance of a jet vane under nozzle exhaust conditions. [10]

Murty and Chakraborty [14] made numerical analyses to understand a jet vane thrust vector system of a tactical missile by solving three-dimensional Reynolds Averaged Navier-Stokes(RANS) equations with $k - \epsilon$ turbulence model and the solid walls were predicted with a standard wall function. They also made a correlation study to predict side and axial force, and roll moment with different chamber pressure and vane deflection angles. They created the correlation model that the force generation of the jet vanes could be obtained without performing a large number of tests using the model.

Giragosian [15] also mentioned the theoretical background of complex flow around the jet vane by using linearized supersonic aerodynamic theory. It was mentioned in this paper that the jet vane test settlement is orthogonal and little interactions were measured during the static solid rocket motor firing tests with the jet vane.

Hamel, de Champlain and Kretschmer [16] validated a computational fluid dynamics (CFD) design tool with a wind tunnel test to simulate flow around a jet vane. They made their tests for two different supersonic velocities and several angles of attacks. They used Particle Image Velocimetry (PIV) to capture shocks around the vane. They used the finite volume discretization of the Navier-Stokes equations with the $k - \epsilon$ standard turbulence model and the implicit solver as a CFD method. The method and the PIV measurements around the jet vane give a very similar flow structure around the jet vane.

Rainville, deChapmlain and Kretschmer [17] have also carried out extensive work on a jet vane TVC system. They divided their study into three parts; wind tunnel test on a scaled jet vane model, CFD modeling and actual rocket motor test such that the force acting on the jet vanes can be measured. Their study also gives information

about the jet vane aerodynamic surface material. The vane which they used in their study, was made of copper infiltrated tungsten (CIT), and the material and combusted gas interaction was examined. Temperature changes on the jet vane and erosion of the jet vane control surfaces are included in their study. They validated their CFD simulations it with force and temperature measurements around the jet vane.

In another study, tests were carried out by using SRMs and jet vanes at the actual scales [5]. In this study, the jet vane is examined to obtain aerodynamic coefficients as well as the ablation characteristics. Some jet vanes were produced with different types of refractor materials such as molybdenum and tungsten. The test motor was placed in an upright position to the thrust measurement system and the measurements were carried out. They measured force from ablating jet vanes and improved the correlation method to predict the area changes of the jet vanes that were produced from different materials.

In order to visualize the complex flow conditions of nozzle and thrust vector control systems, literature reviews are done. In the literature reviews, it is seen that the Schlieren visualization technique is generally performed for compressed air setup with the converging-diverging nozzle to visualize the flow. The Schlieren visualization system, as understood from all these literature reviews, is used to examine plume structure [18–20]. In the case of solid propellant rocket engine or liquid fuel rocket engine ignition tests, the plume structure formed in hot flow is also examined with Schlieren system [21]. In addition to the nozzle plume visualization, cold flow nozzle with thrust vector control systems are examined together. In a study, experiments took place in a supersonic indraft type wind tunnel in which nozzle exit and jet deflector are structured as 2D [27]. Most of the surveyed literature is about cold flow implementing the converging nozzle studies are performed on nozzle plume and rocket nozzle secondary injection thrust vectoring. Most of the surveyed literature is about cold flow implementation on a converging nozzle to investigate nozzle plume and rocket nozzle secondary injection thrust vectoring. The effect of TVC systems on plume, such as secondary injection and jet deflectors, has been generally studied with the Schlieren visualization system [22].

In the literature, theoretical studies of a supersonic wing guide us to understand the

structures of the complex flow on a jet vane [23–25]. Moreover, numerical analyses and experimental studies on a jet vane gives detailed information of the flow around the jet vane. In these studies, Static Pressure and Mach number distributions on jet vane were obtained. The detached bow shock wave occurs before the jet vane leading edge and expansion wave and oblique shock can be seen at the concave and convex surfaces of the vane, respectively. [26]. However, the literature survey shows that numerical studies are required to be verified by tests, such as wind tunnel tests and static ignition tests [17, 27, 28]. The forces produced by a jet vane at static firing tests are the actual forces that the jet vane can produce. The static firing tests and the wind tunnel tests are very costly, but all these tests constitute an essential basis for the verification of CFD solutions.

1.4 Thesis Objective

The objective of the present study is to develop a solution method to find aerodynamic performance parameters of a jet vane, which is placed at the exit of the nozzle of an SRM, in order to use during design studies of the jet vane control surface. The flow over a jet vane of a thrust vector control system is investigated using the numerical technique. Three dimensional, unsteady and viscous flow over the jet vane has been solved numerically, in which the interaction of high temperature and high speed exhaust gas flow with the jet vane is examined in detail. In addition, static firing tests of a rocket motor, which contains jet vanes at the nozzle exit plane, are conducted in the static rocket motor stand of TÜBİTAK-SAGE. The thrust and the side forces due to the jet vane are measured for the different angle of attack values to validate the CFD approach. The nozzle shock pattern in the presence of the jet vane is also visualized by using the Schlieren technique.

In this thesis, Chapter 1, TVC systems are presented. The basic operating principles of the TVC systems and the types of TVC are introduced and the details of the jet vane TVC system are given. The jet vane TVC system is placed at the exit of an SRM. Therefore, the solid propellant rocket motors are mentioned in a general way and performance parameters in static ignition tests are briefly mentioned. In Chapter 2, numerical and experimental setups are described. In Chapter 3, simulation results

and test results were examined in detail for different vane angles.

CHAPTER 2

NUMERICAL AND EXPERIMENTAL METHODS

2.1 Introduction

A jet-vane thrust control system is studied both numerically and experimentally in this thesis. The flow field about a rocket nozzle with a jet vane was solved by the use of a commercial computational fluid dynamics (CFD) solver Ansys FLUENT. Three-dimensional Reynolds-averaged Navier-Stokes equations were employed and simulations were performed for four cases, for which the jet vanes are positioned at 0°, 10°, 20° and 30° angles of attack.

In addition to numerical simulations, static firing tests of a small-scale rocket motor with a jet vane model were conducted. In these experiments, pressure and force measurements, and flow field visualizations were performed. The results of these measurements are used to verify the results of the numerical simulations. In this chapter, numerical and experimental setups and related methodologies are described in detail.

2.2 Nozzle and Jet Vane Geometry and Boundary Condition

In supersonic flows, the double-wedge type airfoil profile is generally used (Figure 2.1). The airfoil has sharp leading and trailing edges, so in a supersonic flow, oblique shocks and expansion waves are formed on the double-wedge airfoil. Drag and lift on the wing can be predicted by the use of analytical methods [15]. The analytical methods are shock-expansion theory and linearized supersonic theory can be used to predict lift and wave drag.

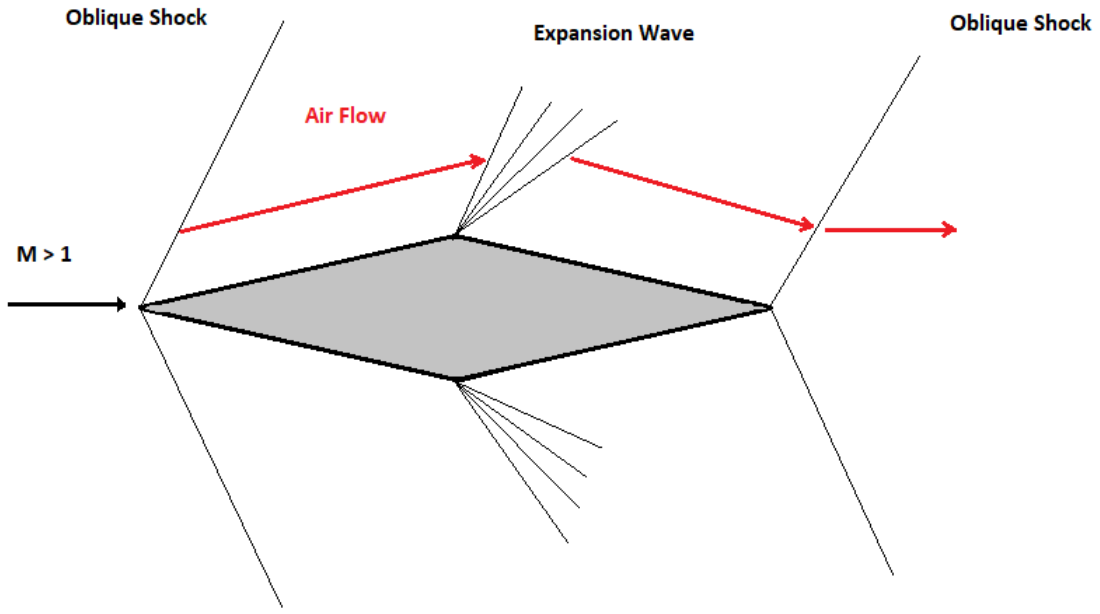

Figure 2.1: Shock structure on double-wedge type airfoil

Usually, leading and trailing edges of jet vanes which are used in TVC systems are rounded in order to reduce aerodynamic heating at high speeds and to prevent thermal ablation at the leading edge of the vane. The combustion gas passing through the jet vane already has a high temperature and a high velocity. Moreover, it contains highly oxidative materials that may cause mechanical, thermal and chemical ablation. After rounding the edges, the shock on the wing will be a bow shock wave, as shown in Figure 2.2.

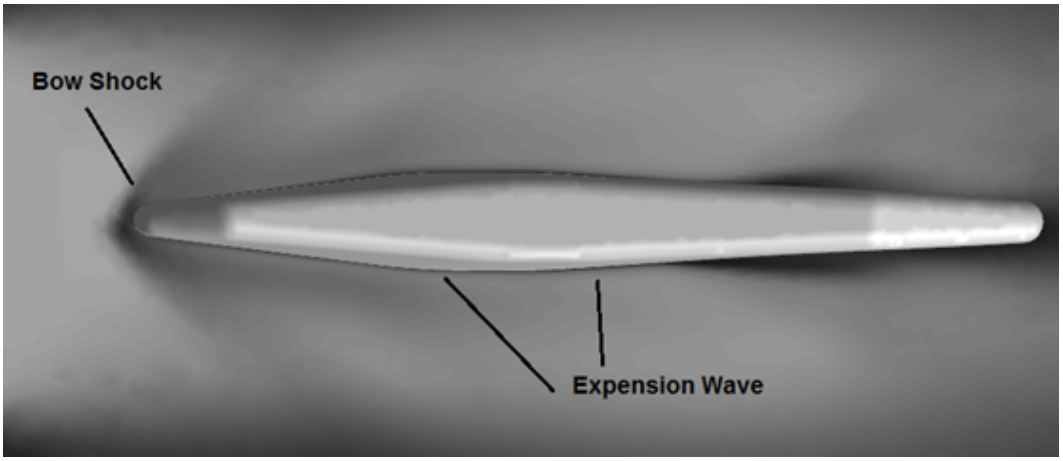

Figure 2.2: Jet vane shock interaction

The jet vane is designed to produce high lift with low drag at nozzle exit flow conditions. For this purpose, a jet vane was designed and some sketches are shown in Figure 2.3. Despite the increase in the wave drag, aerodynamic heating at high speeds is reduced and thermal ablation is prevented.

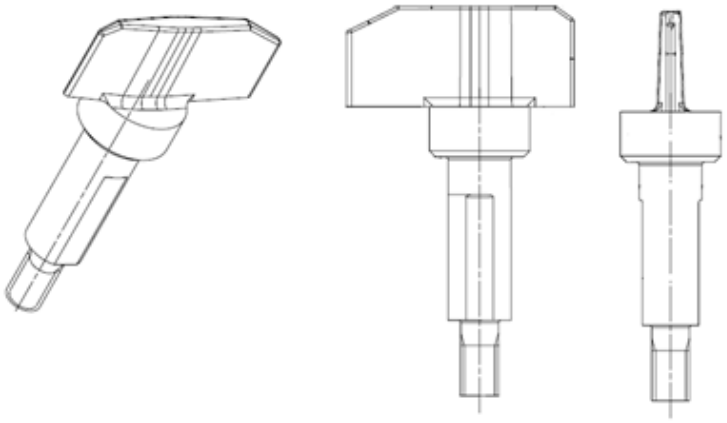

Figure 2.3: Jet vane drawing

The jet Reynolds number at the nozzle exit based on the bulk velocity is approximately $1.8x10^4$. The high Reynolds number flow passes over the jet vane that is placed just at the exit of the nozzle. Flow properties, the interaction between the nonlinear shock wave and the jet vane can be analyzed by using numerical approaches.

Figure 2.4, shows the nozzle and the jet vane fitted to the small-scale rocket motor,

which will be described in detail subsequently. A jet vane was manufactured for this study and molybdenum was chosen as the jet vane material. The setup was constructed to hold and position the jet vane downstream of the existing nozzle in the jet vane-nozzle test assembly.

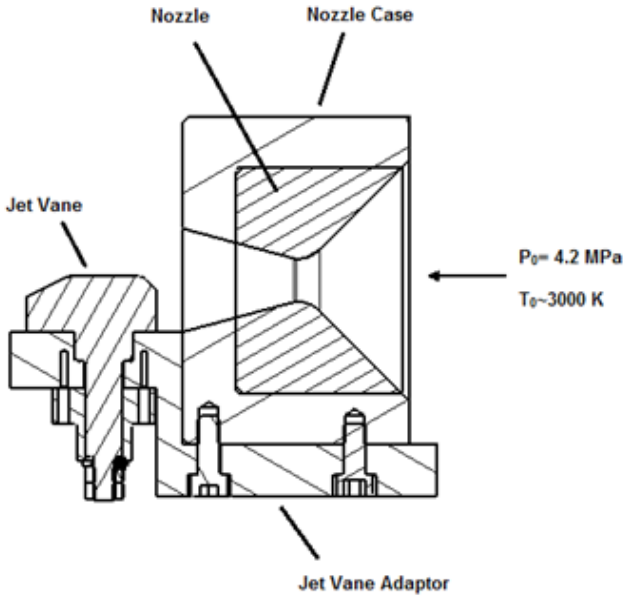

Figure 2.4: Nozzle-jet vane assembly

The combustion gas enters the convergent−divergent nozzle inlet. The properties of the combustion gas are estimated by using the Chemical Equilibrium Analysis tool of NASA (NASA CEA). Total pressure and total temperature of the gas are also defined for the inlet boundary condition. Combustion gases are defined as compressible flow systems with ideal gas assumption such that it can be analyzed by using the energy, continuity, momentum and state equations. Compressible flows are usually characterized by the total pressure P_0 and total flow temperature T_0 of the flow. For an ideal gas, these quantities can be linked to the static pressure (P), the static temperature (T), Mach number (M) and the ratio of specific heats (γ) by the following equations [9]:

$$\frac{P_0}{P} = (1 + \frac{\gamma - 1}{2} M^2)^{\frac{\gamma}{\gamma - 1}} \tag{2.1}$$

$$\frac{T_0}{T} = (1 + \frac{\gamma - 1}{2} M^2) \tag{2.2}$$

These relationships describe the variation of the static pressure and temperature in the flow as the Mach number changes under local isentropy conditions. Also, the ideal gas law is written in the following form:

$$\rho = \frac{p}{\frac{R}{M_\omega}T} \tag{2.3}$$

CFD analyses are used to calculate the effects of flow elements such as shock interactions and temperature changes, which are not easy to observe by means of measurements. In this context, a three dimensional solution domain was created for solid rocket motor and the jet vane. Then, the solution domain was meshed according to the solver selected for this solution domain. The computational domain for the nozzle jet vane assembly is given in Figure 2.5.

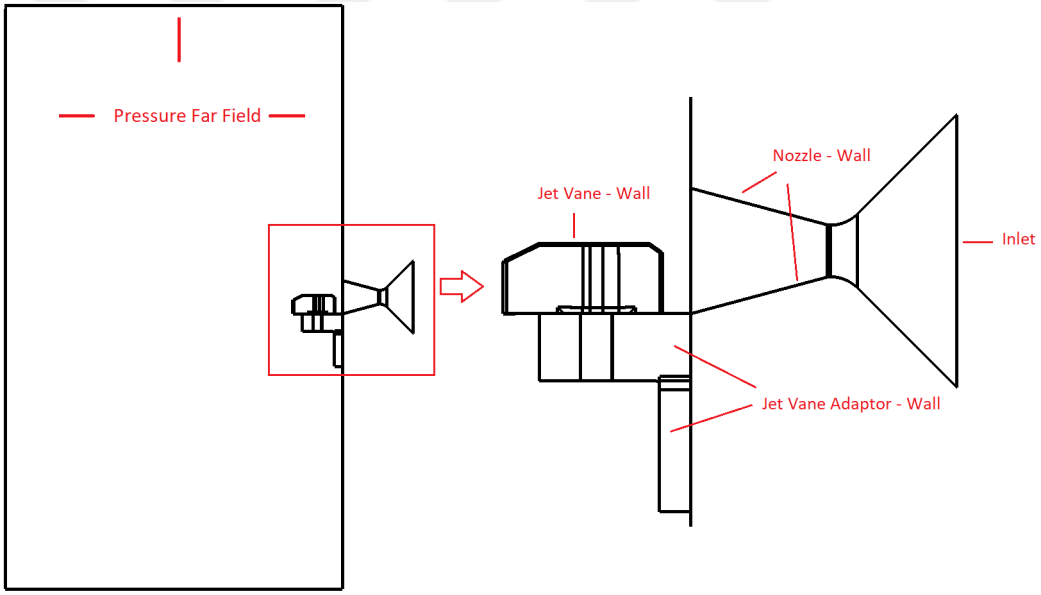

Figure 2.5: Computational domain and boundary conditions (pressure far field, inlet and walls

The pressure inlet conditions of the numerical analysis were obtained from the experiments. The base value of the combustion chamber pressure was taken from the pressure measurements. The SRM burned gas properties were obtained using NASA CEA. In this program, the combustion gases were accepted as an ideal gas. The total temperature, the specific heat ratio and the molecular weight of the combustion

gases and other chemical and transport properties of these gases were obtained theoretically. The variations of the specific heat, the conductivity and the viscosity values with temperature were tabulated. The obtained gas properties values were used in the numerical analyses to identify the combustion gases. Consequently, the theoretical calculations were found to be sufficient at the preliminary design stage. In addition, the pressure inlet can be verified numerically by taking into account the calculated gas characteristics and the diameter of the nozzle throat.

Table 2.1: CFD inlet and boundary conditions

Inlet Conditions		**Boundary Conditions**	
Nozzle Inlet Pressure (Bar)	42	Far-Field Pressure (Bar)	0.89
Nozzle Inlet Temperature (K)	≈ 3000	Far-Field Temperature (K)	300
Gas	Combustion Gases	Far-Field Gas	Air

Fluent defines inlet and boundary conditions as follows:

- Pressure inlet boundary conditions are applied to define the total pressure, total temperature and flow inlet scalar quantities. In this study, the total pressure value is selected such that the combustion chamber pressure value remains constant after the SRM ignited.
- Pressure far-field boundary condition is usable only for compressible flows. The boundary condition is applied to model a free-stream compressible flow at infinity, with free-stream Mach number and static conditions being specified.

2.2.1 Computational Grid

2.2.1.1 Comparison of Different Mesh Types

The three-dimensional Reynolds-Averaged Navier-Stokes equations with the k-ω Shear Stress Transport turbulence model (SST k-ω model) were implemented to examine differently meshed solution domains. The enhanced wall treatment approaches implemented in the grids boundary layer. For this wall treatment approach, the first cell height of the boundary layer was set to y+ of 1. Using a fine mesh at the boundary layer resolves the turbulent phenomena better in cases such as when shock waves do interact with boundary layers and impose strong pressure gradients on them. The main disadvantage of this approach is that it is computationally expensive ($y+ \simeq 1$).

The flow domain around the vane was discretized by using different types of mesh. In this thesis, the unstructured, structured, hybrid and adaptive grids were implemented. The main advantages and disadvantages of the used grid types were mentioned. The effect of each grid type on the resolution was also investigated. The obtained CFD analysis results were compared with each other. The study was conducted for a jet vane at a zero degree angle of attacks. The same boundary and initial conditions were used in the CFD analyzes and the same turbulence model was selected for all models. The cell sizes around the vane were tried to be kept similar for the different grid types.

In this study, firstly, a three-dimensional solution grid, which is formed of unstructured mesh elements, was studied. The unstructured triangular and tetrahedral grid is simple to create for complex geometries. However, the unstructured grid is not aligned with the stream as good as the structured grid. This misalignment causes inaccuracy when simulating the flow. In order to understand the unstructured grid effect on the simulation, the unstructured mesh element was generated. The jet vane and the jet vane adaptor surface were meshed with relatively small triangular cells, and a smooth transition from surface to flow domain was prescribed. In Figure 2.5, the computational domain can be seen. To get finer grid cells around the jet vane, smaller triangular cells were implemented on the jet vane surface. A close-up view of the mesh around the vane surface and the boundary layer on the jet vane is given in Figure 2.6 and 2.7, respectively.

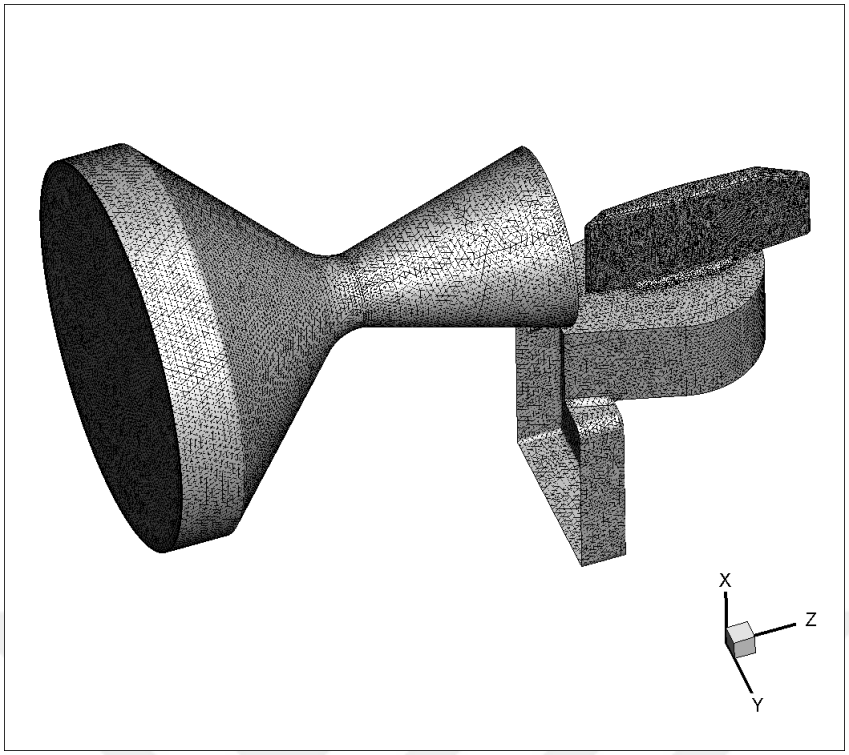

Figure 2.6: Unstructured triangular surface mesh

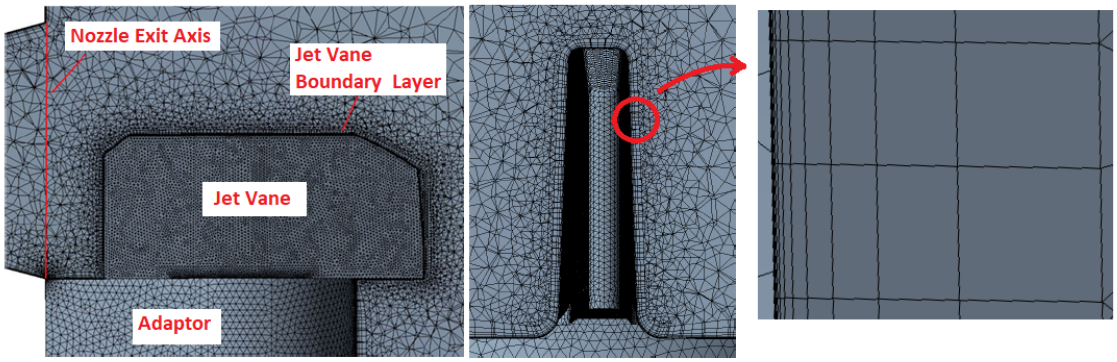

Figure 2.7: Unstructured tetrahedral grid type, centerline slice view of vet vane mesh and boundary layer

Within the scope of the studies, a structured grid was formed by using hexahedral elements and CFD analysis was performed for this grid as well (Figure 2.8, Figure 2.9 and 2.10). The main advantage of hexahedral cells is that they are arrangeable cells to follow the flow pattern. On the other hand, generating and arranging structured grids for accurate simulations about complex three-dimensional geometries is a tricky subject.

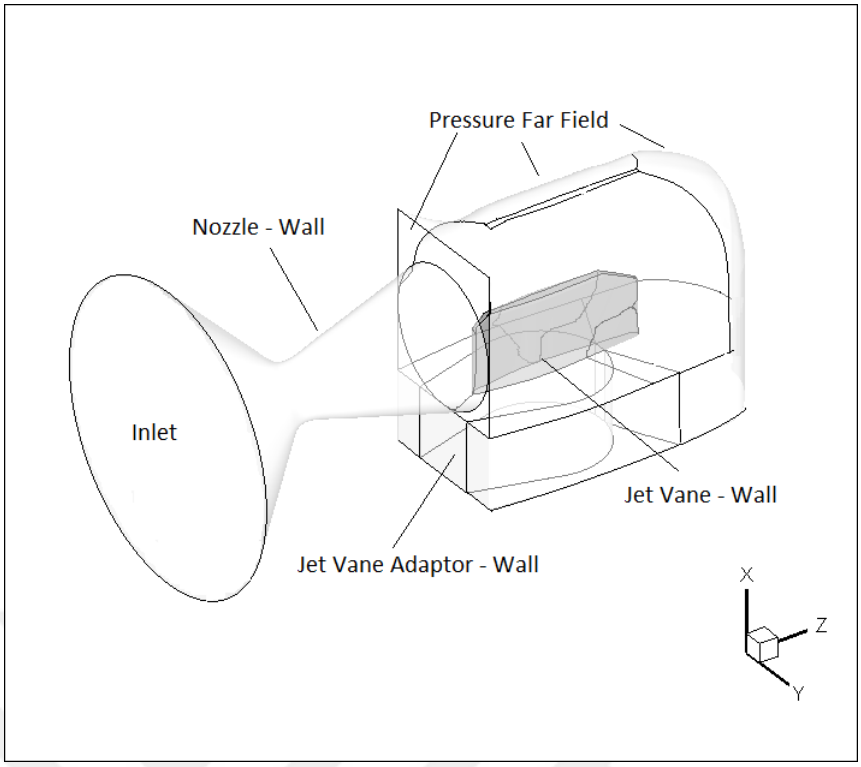

Figure 2.8: Domain for structured mesh

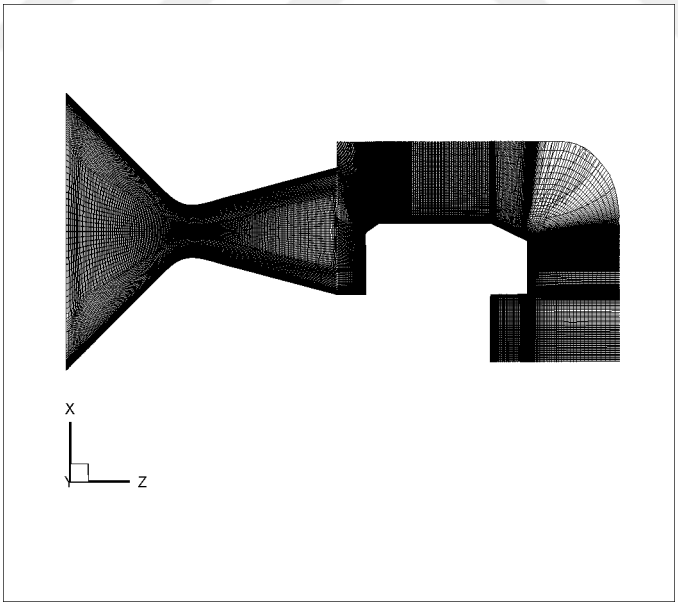

Figure 2.9: Structured hexahedral mesh

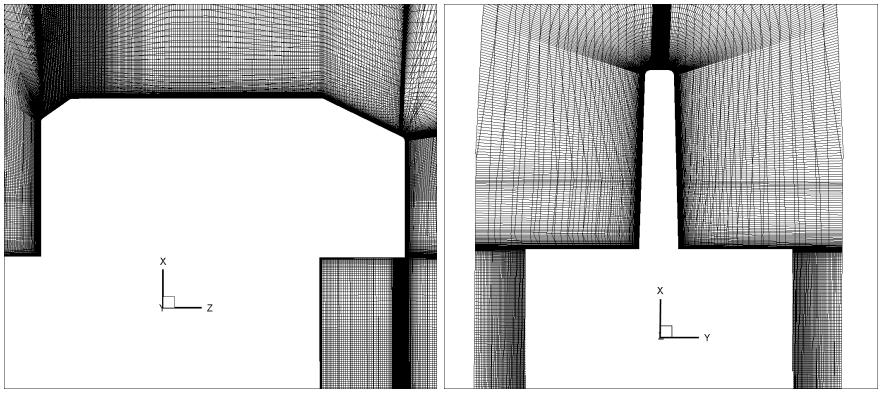

Figure 2.10: Hexahedral grid on jet vane - side and front view

In addition to the tetrahedral and the hexahedral grid studies, a solution domain (Figure 2.11) was discretized with a hybrid grid. In the hybrid grid, the nozzle and the jet vane surfaces were meshed with quadrilateral elements; the nozzle volume was meshed with hexahedral elements, the flow domain was meshed with tetrahedral elements as shown in Figure 2.12 and 2.13. The vane surface has a rectangular grid and the boundary layer around the vane was modeled with a pyramid grid. The advantage of the hybrid grid is the tetrahedral grid in the inviscid part domain and the use of a pyramid grid in the viscous part of the flow domain. Therefore, the boundary layer can be modeled more accurately than the unstructured tetrahedral grid.

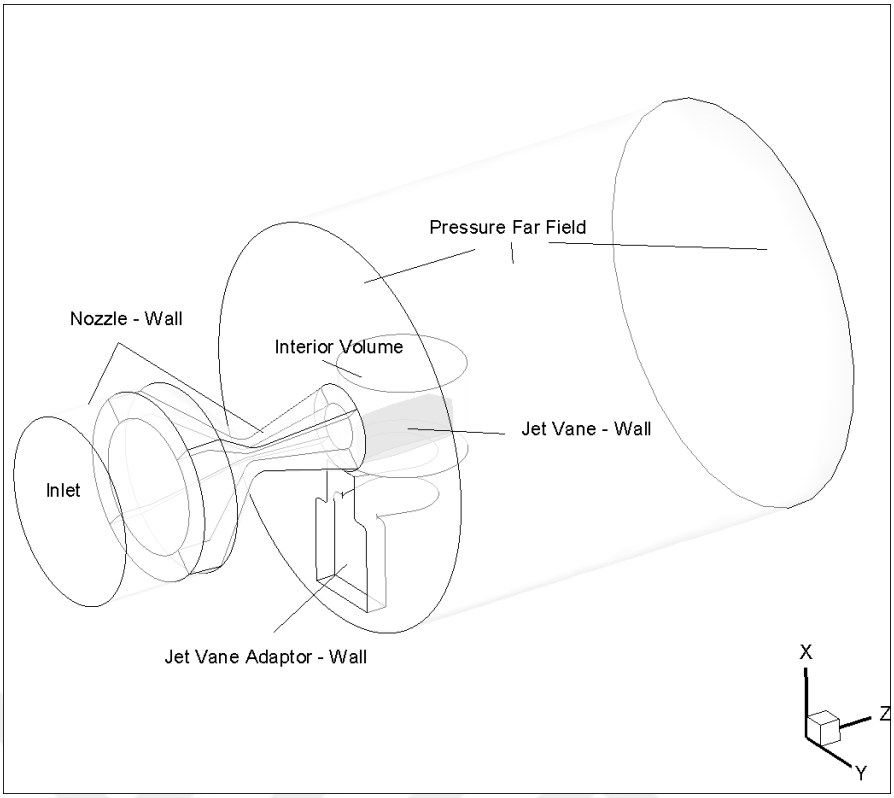

Figure 2.11: Domain for hybrid grid

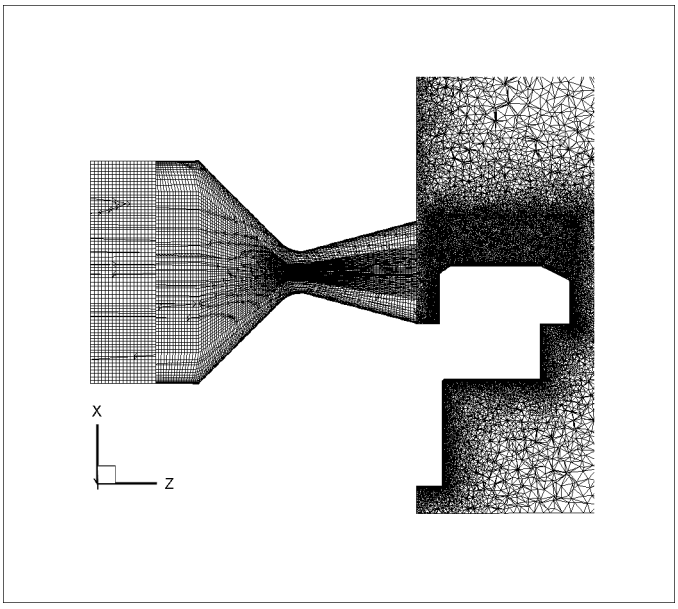

Figure 2.12: Hybrid mesh

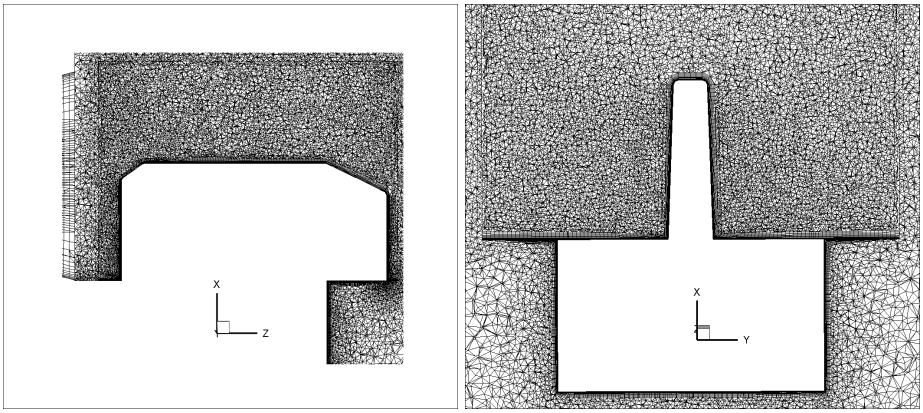

Figure 2.13: Hybrid grid on jet vane - side and front view

Different types of grids are examined and the domains and Mach number contours:

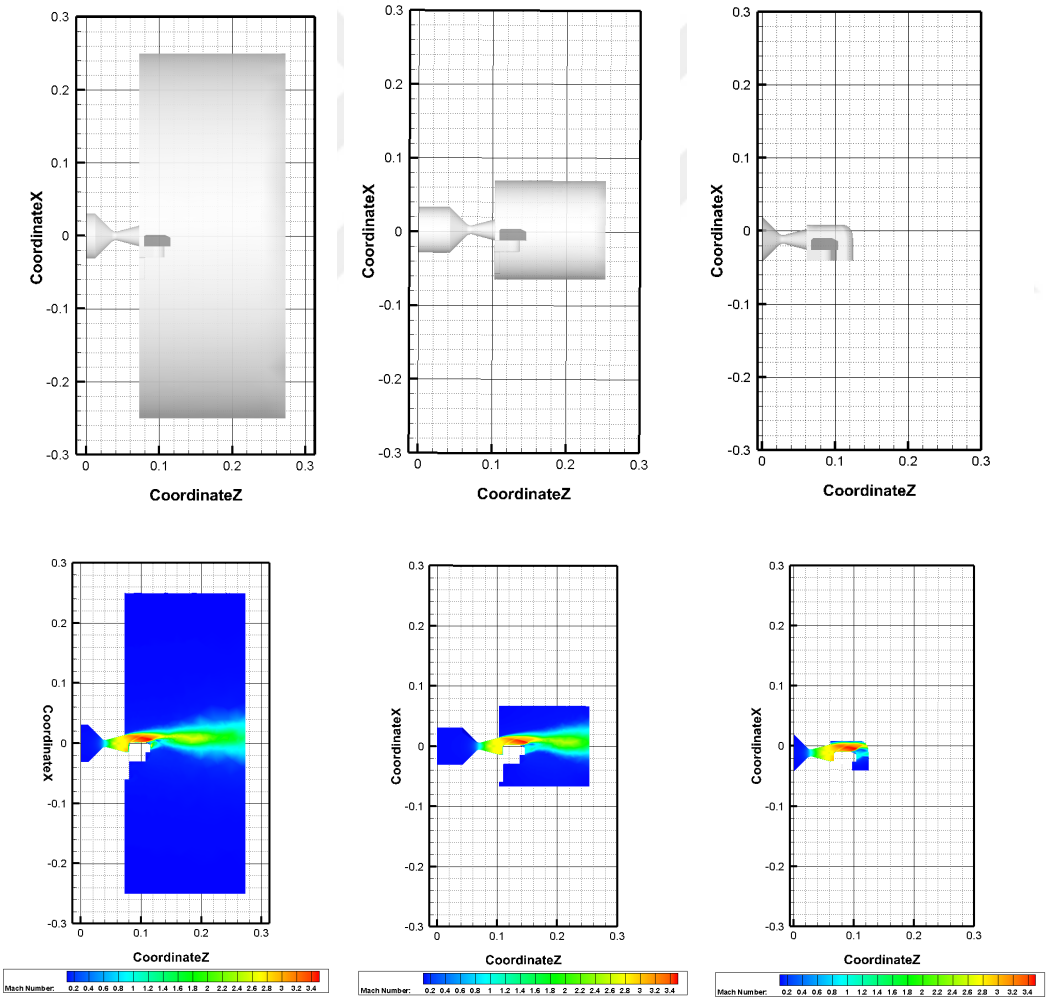

Figure 2.14: Domain and Mach number of section view of the jet vane - (Left to right tetrahedral, hybrid and hexahedral meshes)

In this part of the study, the solution grid using the tetrahedral adaptive mesh approach was reconstructed to use the adaptive mesh approach, Figure 2.15. Mesh adaptation updated according to the change of pressure gradient. With the adaptive grid, the shock zones can be captured more accurately as shown in Figure 2.16. The flow formed on the vane was solved in more detail. Although cell adaptation extends some amount of solution, the results are highly consistent with the test results.

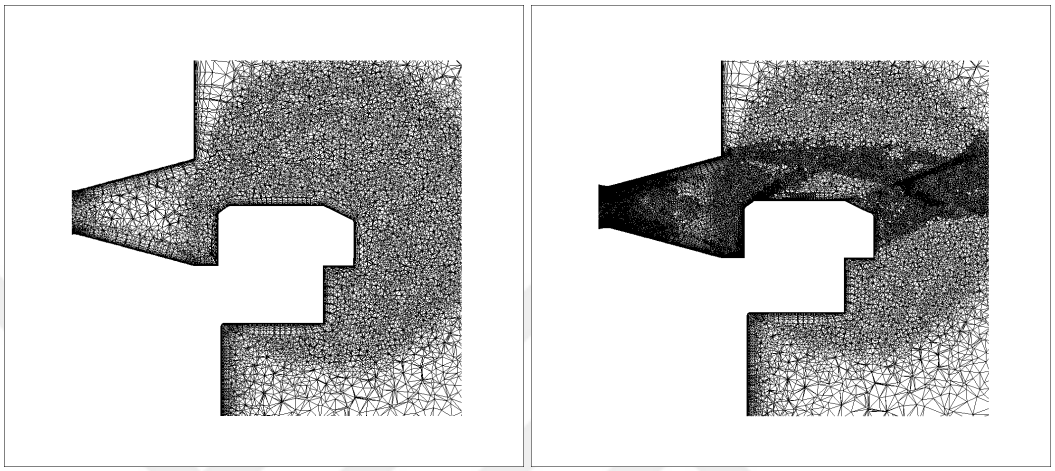

Figure 2.15: Tetrahedral and adaptive tetrahedral grid

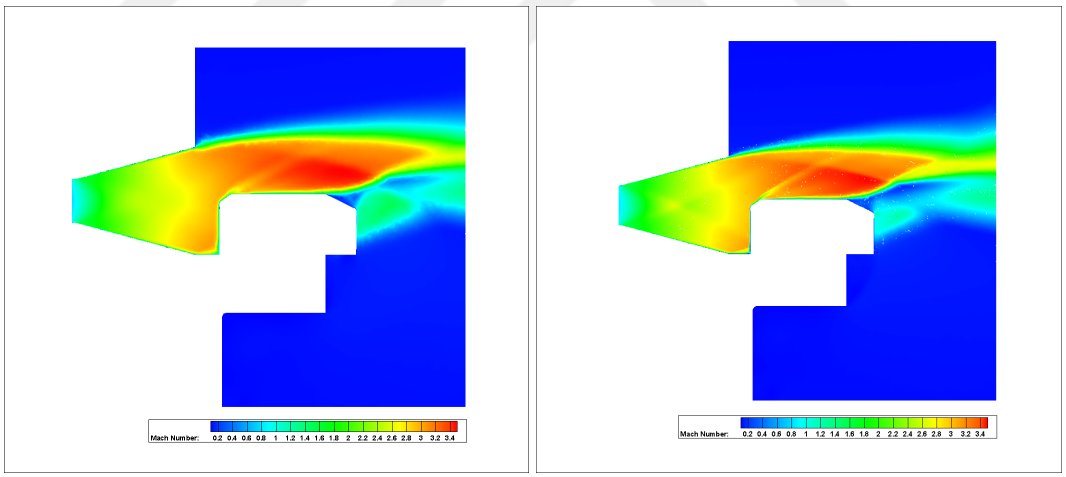

Figure 2.16: Mach contours of tetrahedral (Left) and adaptive tetrahedral (Right) mesh

The comparison of the results that were obtained in the mesh examination study is given in Table 2.2. In spite of the fact that some of the test results are very close to the numerical analysis results obtained with hexahedral mesh, meshed with adaptive tetrahedral grid results are also very close to each other and severe loss of time is prevented.

Table 2.2: Comparison of drag forces

Cell Type	Drag (N)	Experimental Drag (N)	% Relative Difference
Tetrahedral	18.541	17.38	6.263741
Hexahedral	17.531		0.868814
Hybrid	18.069		3.964327
Adaptive Tetrahedral	17.754		2.151899

When the grid effect is examined, it is clear that the solution domain modeled with the hexahedral elements gives the closest result. However, meshing with the hexahedral and hybrid element type takes too much time. This loss of time increases with the complexity of geometry. It is crucial to reduce the loss of time in places where engineering studies are performed. The adaptive grid was chosen as the solution grid to be used in the numerical simulations due to its ease of application and the adaptive grid gave the second-best result in the computational grid study.

2.2.1.2 Mesh Independence Study

The adaptive tetrahedral grid was established and then the grid convergence study was performed until the results of the analyses were independent of the changes in the number of grid points. In order to examine the effect of the grid on the numerical simulations, the jet vane at the angle of attack of 0 degrees first meshed with a grid of 1.2 million cells. The lift and drag were obtained. Grid cell size was then reduced near the jet vane while keeping the first cell height the same. The number of cells in the solution volume was increased to 3, 4, 8 and 10 millions, respectively and the steady-state analyses with SST k-ω turbulence model were performed using these grids. The change in lift and drag force values of the meshes for the different number of grid cells were found and compared to the force values obtained from the test result of the jet vane at 0 degree AoA. Comparison of the results are given in Table 2.3.

Mesh with 10 million grid cells was selected and analysis continued. Although this cell number prolonged the solution time, it gave very close results with the experiment result.

Table 2.3: Unstructured solution grids comparison of computation cost

AoA (deg.)	**Turbulence Model**	**Grid Element Number (M)**	**Calculation Time**	**% Differences**
0	SST k-ω	≈ 1.2	14 (hr)	8.29
		≈ 3	25 (hr)	6.62
		≈ 4	1.5 (day)	6.27
		≈ 8	5 (days)	3.43
		≈ 10	10 (days)	2.15

2.2.1.3 Solver and Turbulence Models

The treatment of turbulence in the Reynolds-Averaged Navier-Stokes (RANS) equations is at the center of most practical Computational Fluid Dynamics (CFD) approaches. The hypothesis behind the RANS equations (also called Reynolds decomposition) is that the time-dependent turbulent velocity fluctuations can be dissociated from the mean flow velocity. The functions of the velocity fluctuations, known as the Reynolds stresses, require a turbulence model (e.g., the two-equation k-ϵ and k-ω models) to produce solvable equations for a close system [29].

In order to determine the turbulence model to be utilized in this thesis, specific analyses have been performed. There are many methods for turbulence modeling in the Fluent program. As referred to in the literature study, the k-ϵ realizable model has frequently been applied as the turbulence model in nozzle and thrust vector applications [12]. Despite the relatively low demand in computational cost in many engineering applications, consistent results have enabled the use of the k-ϵ realizable turbulence model in many subject fields. Besides this model, the k-ω model was also used for the numerical analysis. The k-ω model has a success of capturing shock interactions with shock and boundary layer. The three dimensional Reynolds-Averaged Navier-Stokes equations with the k-ω Shear Stress Transport turbulence model (SST k-ω model) were also used to solve the thesis problem. The SST k-ω model has refined the model regarding the standard k-ω model.

In these studies, while solution times and computational load are not taken into account, the compatibility of the results with the test is taken into consideration. The mentioned turbulence models are used for the vane at 0 and 20 degrees. The adaptive tetrahedral solution grid is selected as the solution domain mesh. The element number is 10 million and adaptation regarding pressure gradient continued until each drag force values between iteration less than % 0.1.

The outcomes of the numerical analysis are compared in Table 2.4 and Table 2.5 and the turbulence model compatible with the test is selected as the SST k-ω model which provide best approximation to the experimental results.

Table 2.4: Comparison of numerical analyses with realizable k-ϵ and test results

	Numerical analysis k - ϵ Realizable		**Test**		**% Difference**	
AoA (Deg.)	**Lift (N)**	**Drag (N)**	**Lift (N)**	**Drag (N)**	**Lift(N)**	**Drag(N)**
0	0	18.34	0	17.38	0	5.52
20	101.8	56.44	121.4	50.25	16.15	12.32

Table 2.5: Comparison of numerical analyses with SST k-ω and test results

	Numerical analysis k - ω SST		**Test**		**% Difference**	
AoA (Deg.)	**Lift (N)**	**Drag (N)**	**Lift (N)**	**Drag (N)**	**Lift(N)**	**Drag(N)**
0	0	17.75	0	17.38	0	2.15
20	112.4	46.83	121.4	50.25	7.41351	6.81

The numerical studies are carried out in order to obtain the computed flow fields for all cases (0°, 10°, 20°, 30° angles of attacks). For the numerical study, commercially available ANSYS software is used to compute the three-dimensional flow field. Reynolds-Averaged Navier-Stokes equations are solved along with the k-ω Shear Stress Transport turbulence model. The considered turbulence models have been utilized in the adaptive tetrahedral grid for the different angles of attacks. y^+

values on the jet vane are less than 1. Second order upwind discretization is employed for flow and turbulence computations for higher accuracy. For the first and second-order coupled solver of the numerical scheme simulations, the convergence of a solution must be determined well in order to get the correct lift and drag values of the jet vane. Convergence is often measured by the change of residuals of the flow field parameters such as continuity, x, y and z velocities, momentum and energy with turbulence quantities k and ω.

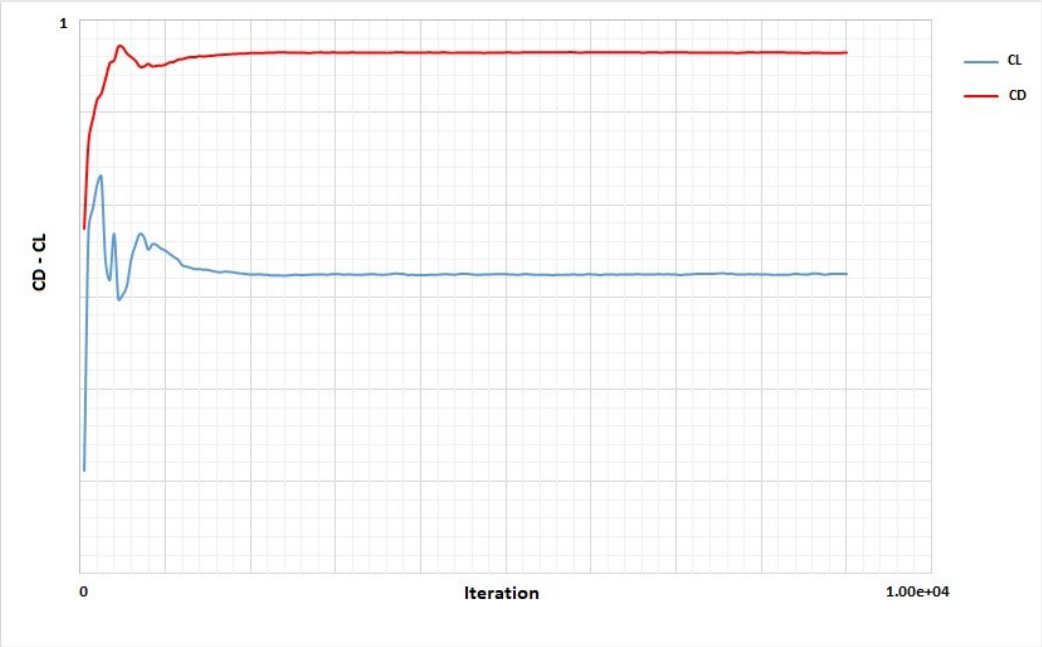

Figure 2.17: Change of lift and drag coefficient value with iteration

In addition to all, the lift and the drag coefficients and the mass balance between nozzle inlet and outlet are also checked for convergence (Figure 2.17). The simulations are accepted as converged when the lift and drag coefficients are not changing and mass flow rate differences between nozzle throat and nozzle inlet reached 10^{-4} kg/s between consecutive iterations.

2.3 Experimental Setup and Methods

The performance of a solid propellant rocket motor can be investigated with a number of tests. The SRM performance can also be obtained by using different simulation

tools. However, a test provides more valuable data even though the test cost is high. The performance parameters of a SRM is provided by static firing tests. In the static firing test, the SRM is ignited after mounting the motor on a test bench. Time variation of thrust and pressure are the leading performance parameters of the SRM and the data are obtained from this static firing test. TÜBİTAK-SAGE has experiences with the design and test of solid propellant rocket motors. Full-scale solid rocket motor and Ballistic Evaluation Motor (BEM) can be tested at TÜBİTAK-SAGE. The BEM is a small-scale test motor that is basically used for verification of solid propellant properties. However, in this study, BEM is used with the jet vane to test and obtain the vane characteristics. BEM technical drawing can be seen in Figure 2.18. BEM contains nozzle, nozzle case, solid propellant and propellant case, igniter and sensor adapters.

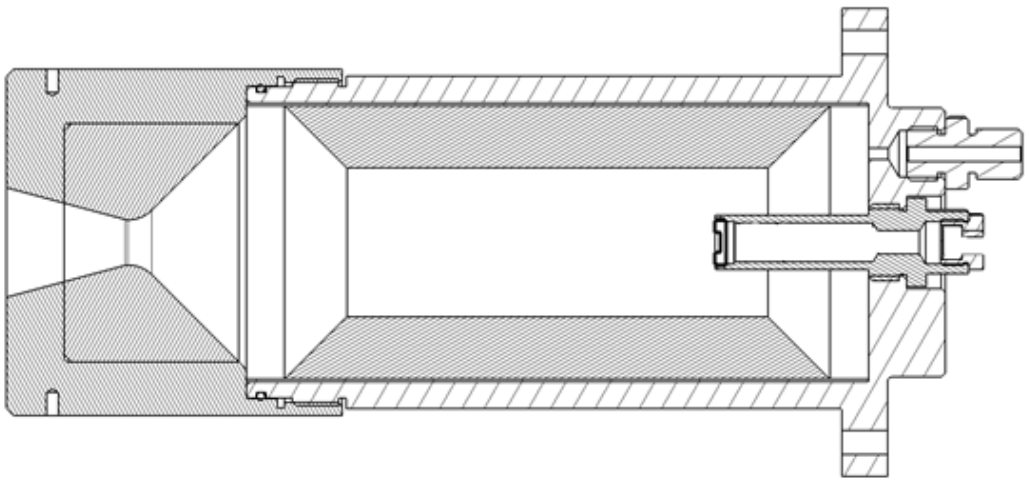

Figure 2.18: BEM technical drawing

The solid propellant regresses from its surface when it is running. The propellant regression in unit time is a crucial parameter of SRM and called as the burning rate. The burning rate of solid propellants is dependent on running conditions such as the pressure in the combustion chamber. The combustion chamber pressure is a substantial factor affecting the burning rate. The selected motor and the burning rates of the propellant at demanded burning rate/pressure are obtained by specific nozzle throat diameter. A certain nozzle diameter is used for this study.

2.3.1 Experimental Model

In this thesis, subscaled SRM (Ballistic Evaluation Motor-BEM) internal flow CFD analysis was made by using a subscale jet vane which was designed in TUBITAK SAGE. Moreover, comparative analysis and validation of the numerical simulations with the results obtained from the static firing tests of the BEM-jet vane were performed. The lift and drag produced by a jet vane placed at the exit, in radial axis of the SRM nozzle were obtained with static firing tests. The aerodynamic properties of designed jet vane were found for the actual flow conditions. Figure 2.19 shows the technical drawing of BEM with jet vane.

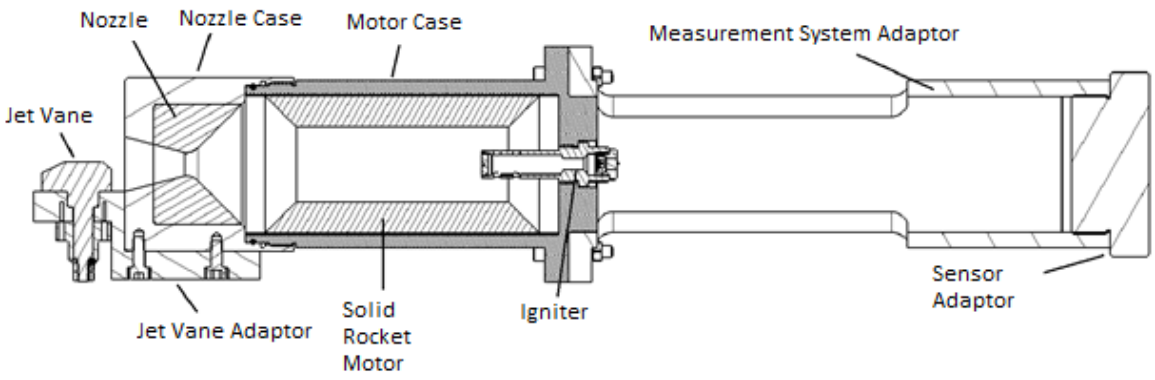

Figure 2.19: Solid rocket motor, nozzle and jet vane technical drawing

In the design phase of the rocket motor and the TVC system, performance tests were carried out with real-scale static motor firing setup. In these tests, axial thrust, side force and roll torque were measured.

In Figure 2.20, SRM parts were gathered for the integration process (a SRM case, a nozzle and nozzle case, a solid propellant with a steel liner.) Generally, composite propellants are used with metal liners. The liner is used for pouring the liquid phase propellant into it, and then propellant and liner bonds together after the propellant cool down. After quality control tests are done for propellants such as X-ray photography and geometrical measuring, the propellant can be used in the BEM tests.

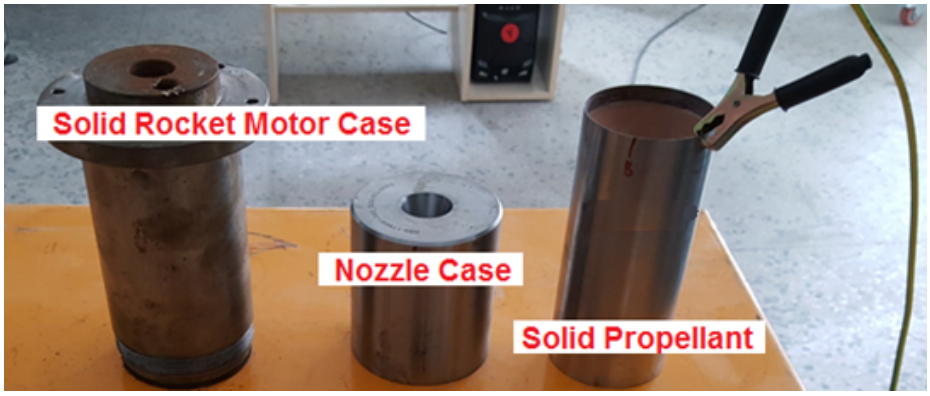

Figure 2.20: Ballistic Evaluation Motor parts

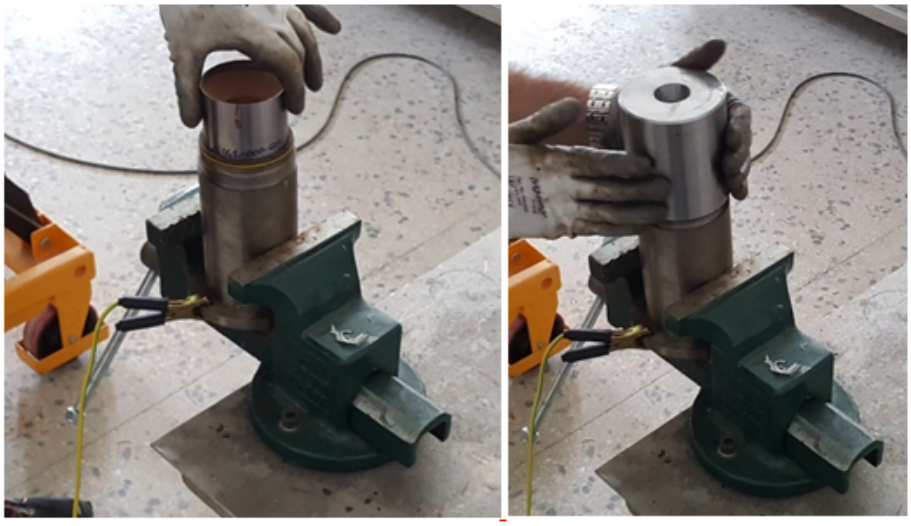

Figure 2.21: Assembling the BEM

Nozzle case integration process was taken and integrated with the motor case using mechanical tooth interface as shown in Figure 2.21. After nozzle case was assembled, jet vane adaptor and jet vane were bolted the nozzle case.

Figure 2.22: Jet vane takes place on nozzle exit plane

After the experimental model was prepared, the complete system was taken to the test bench. At the test bench the pressure transducer and ignitor were assembled to the rocket motor case.

At the end the BEM with jet vane was connected to the Multi-Dimensional Thrust Measurement System (Figure 2.23). The system was carefully aligned in order to get test data without any misalignment issues.

Figure 2.23: Test bench alignment

2.3.2 Experimental Setup and Force Measurement System

The solid rocket motors are tested statically to analyze the performance of solid propellant based upon thrust generated. Measurements related to performance and reliability of thrust systems are necessary at the stages of Solid Rocket Motor development, evaluation and verification. The main variables measured during the static firing tests are the thrust, the combustion chamber pressure and various temperature data. There are various methods for thrust (axial and lateral) measurement such as direct force measurement, measurement of exit properties of exhaust gases and momentum balance establishment. The most common feature of these methods is using direct force measurement that requires a special mechanism. The mechanisms for measuring force which is called Thrust Measurement System are basically composed of a fixed lattice, a mobile carrier system, support columns, load cells and a calibration system.

One of the most important parameters of the SRM static testing is to measure the thrust produced by the SRM. The produced thrust was measured using a Thrust Vector Control (TVC) test system structure with load cells. The forces and moments of the rocket motor were measured during firing with respect to the six degrees of freedom of the test system. The designed stand is capable of measuring axial and lateral (misaligned) thrust components and rolling moment of the rocket motor.

In the design phase of the SRM and the TVC system, performance tests were carried out with static motor ignition which is called ground tests. In these tests, axial thrust, lateral thrust and rolling torque were measured. TÜBİTAK-SAGE developed "Multi-Axis Thrust Measurement System (MATMS)" to carry out these types of measurements [7]. The solid model image of "MATMS" is given in Figure 2.24.

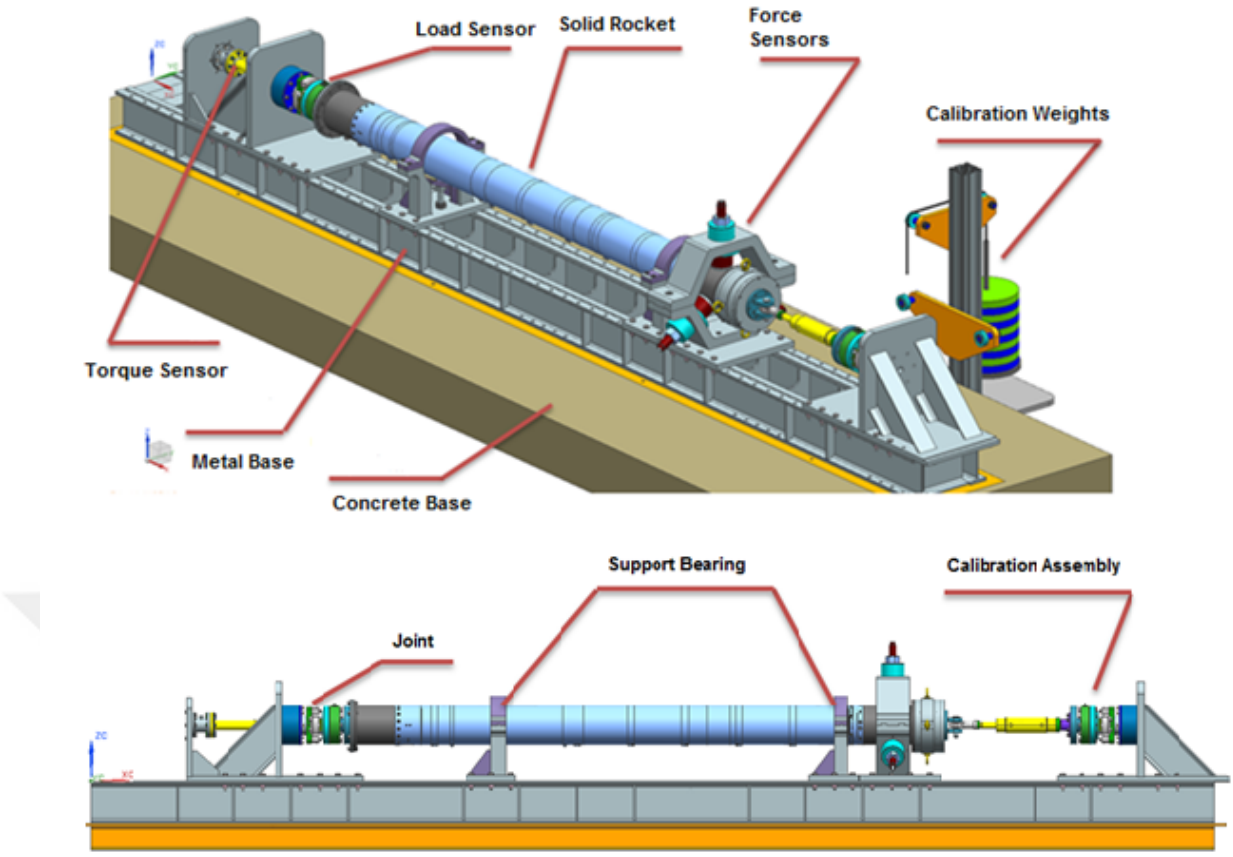

Figure 2.24: Solid model view of MATMS with calibration parts [7]

In the MATMS, torque is measured at the back of the rocket motor and the axial thrust is measured with a 3-component load sensor placed at the back of torque sensor. The lateral thrust values are measured with the hexagon part by 3 load cell standing at 120° with respect to each other (Figures 2.25 and 2.26).

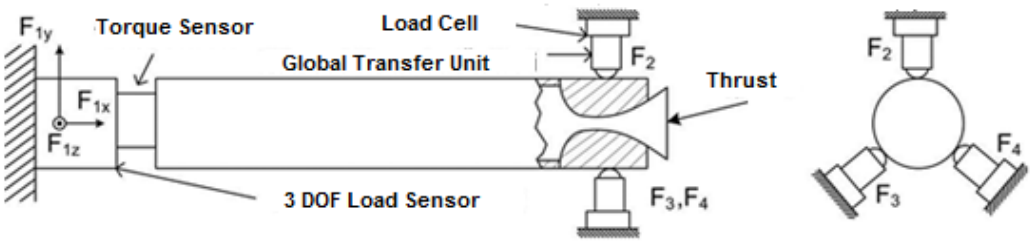

Figure 2.25: Diagram of measurement system, rocket motor and nozzle [7]

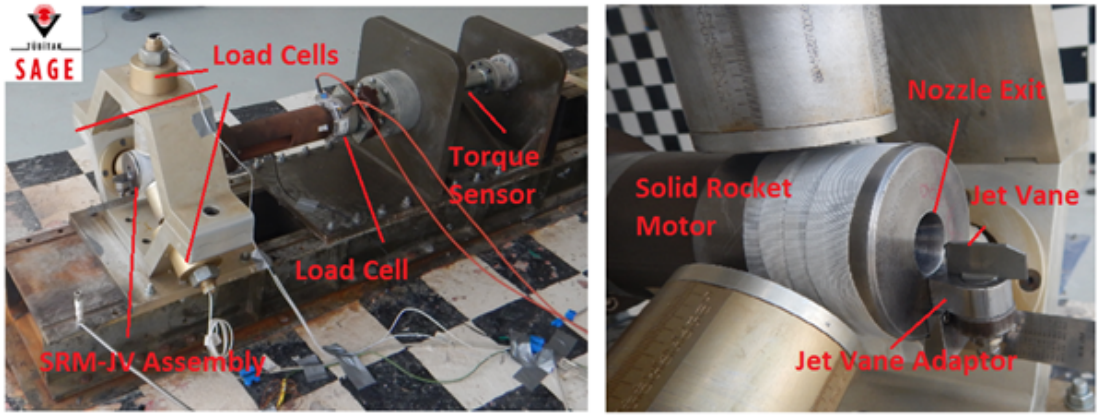

Figure 2.26: SRM-JV assembly mounted on the MATMS

Details of the sensors are given in Table 2.6:

Table 2.6: Properties of sensors

Number	Sensor	Model	Type	Range	Accuracy
1	3 Axis Load Sensor	HBM	U10M	0-50kN	4 % (Full Scale)
1	Torque Sensor	PCB	2301-01A	226 Nm	1 % (Full Scale)
3	Load Cell	OMEGA	LCGB-1 K	455 kg	1 % (Full Scale)

The measurements were made considering the distance between sensors that measure lateral thrust because the vane is on the nozzle outlet axis. The forces generated by the vane are obtained by equalizing the resultant force of the values read from the three force sensors standing at an angle of 120 degrees relative to the hinge on the test system to the moment formed by the jet vane located in the axis of the nozzle outlet. In order to obtain the drag force on the jet vane from static test firings of the solid rocket motor; first, thrust of the rocket motor was measured without the jet vane. Then, a second static firing test of SRM-JV assembly was conducted. Difference between the two measured thrust values gives the drag force on the jet vane.

The alignment of SRM-JV on the MAMTS is highly important. The misalignment of the test part on the test stand and the test stand itself causes measuring incorrect force values and force directions. A whole SRM-JV assembly was connected to the measurement system (MATMS) and before each test a laser tracker was used to align the model. After making the alignment, calibration of the MATMS was performed using

calibration weights. Calibration coefficients were produced and validated in many tests (one of the tests from validation study, Figure 2.27) conducted by TÜBİTAK-SAGE.

Figure 2.27: An image from static firing test

2.3.3 Pressure Measurement and Data Acquisition System

The pressure data was acquired in the SRM combustion chamber to understand the performance of the solid rocket motor. The thrust data also identifies the SRM performance yet pressure and axial thrust data are generally examined together to interpret the performance of components, which are SRM and nozzle. A pressure transducer was used to acquire pressure data at the static firing tests. Kulite XTL-193-190M-210 BARA high-frequency piezoresistive pressure transducer was used for all tests in this thesis. The data acquisition was carried out with IMC CRONOSflex data acquisition system with CRFX/ICPU2-8 IEPE-ICP and universal modules, as shown in Figure 2.28. The data sampling rate was set to 100 kHz.

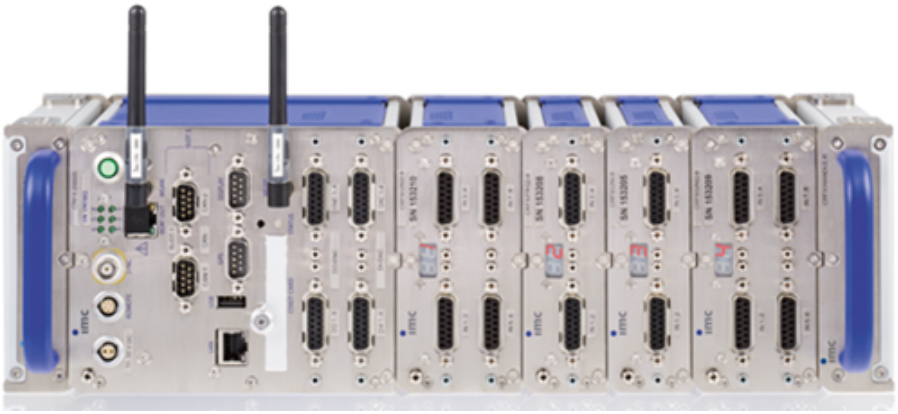

Figure 2.28: IMC CRONOSflex data acqusition system

The plume geometry images were collected during all static firing tests to understand

SRM behavior. Photron SA-X2 high speed camera was used for recording the variations in the plume geometry at 3000 frames per second. A trigger signal was used to synchronize the firing of the SRM and the image recording, such that these processes can start at the same time.

Ambient pressure and temperature were also measured and recorded before each test, which were implemented inthe numerical analysis.

2.3.4 Schlieren Flow Visualization

In the 17th century, Robert Hooke first mentions that, density variation in inhomogeneous media refracts the light passing through. He discusses this phenomenon in his famous book Micrographia. For this discovery he explained many phenomena like the twinkling of stars. Hooke′s original Schlieren system uses two candles, a lens, a human eye and also an observer at the same time. In his book he uses lenses to understand the refraction of the candle plume and the book includes diagram and sketches of refraction of the candle plume, the Fig 2.30 from reenactment of Hookes shadowgraph technique [30].

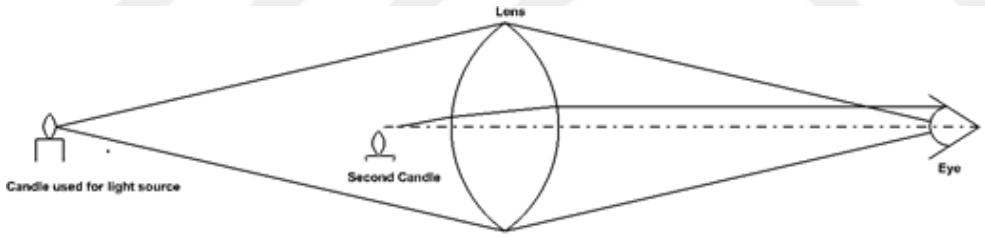

Figure 2.29: Robert Hookes Schlieren system sketch

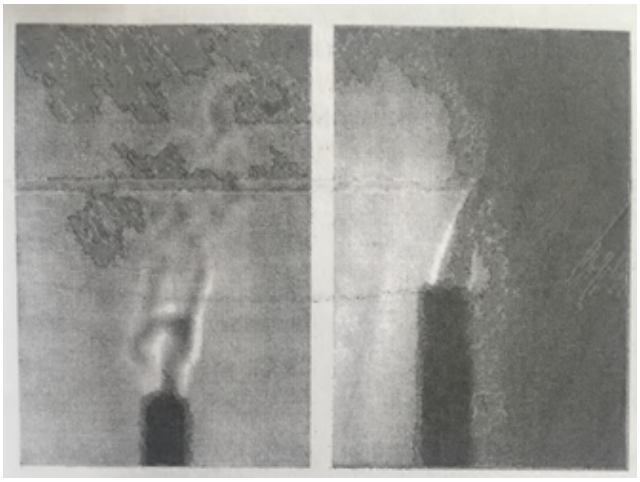

Figure 2.30: Schlieren of a candle

After Hooke, Christiaan Huygens invented a new version of the Schlieren to check glass blanks. He used the Schlieren to look for striae in glasses and nowadays it is called optical shop test. This historical development of the Schlieren continued and in the 19th century August, Toepler re-invested the Schlieren and gave the name that we use today. Toepler′s Schlieren studies were published by Ostwalds Classics of Exact Science. At the same time with Toepler, J. B. Leon Foucault also used a technique, called knife-edge test to check parabolic mirrors, but Toepler focused on the scientific way of this technique. By using scientific way means that Toepler investigated shock waves at first. The Schlieren techniques mostly have been used by scientists and engineers to illustrate shock and expansion wave. So Toepler opened a new field that the Schlieren technique can develop. He managed to visualize the Schlieren image of an electrical spark spherical shock wave in air medium [31].

The scientific side of the Schlieren visualization has improved in years and more scientists started to use this visualization technique such as Ernst Mach and Peter Salcher. Mach and Salcher managed to see and take photograph of the oblique shock waves around supersonic bullet [8]. Mach and Salcher then started to work on supersonic airstream. They made an experiment that compressed air passing through a converging nozzle and they succeeded to get first Schlieren photograph of a supersonic jet as shown in Figure 2.31 [8]. From the beginning of the Schlieren to now, many scientists, engineers and ballisticians have worked on observing supersonic flow conditions and shocks.

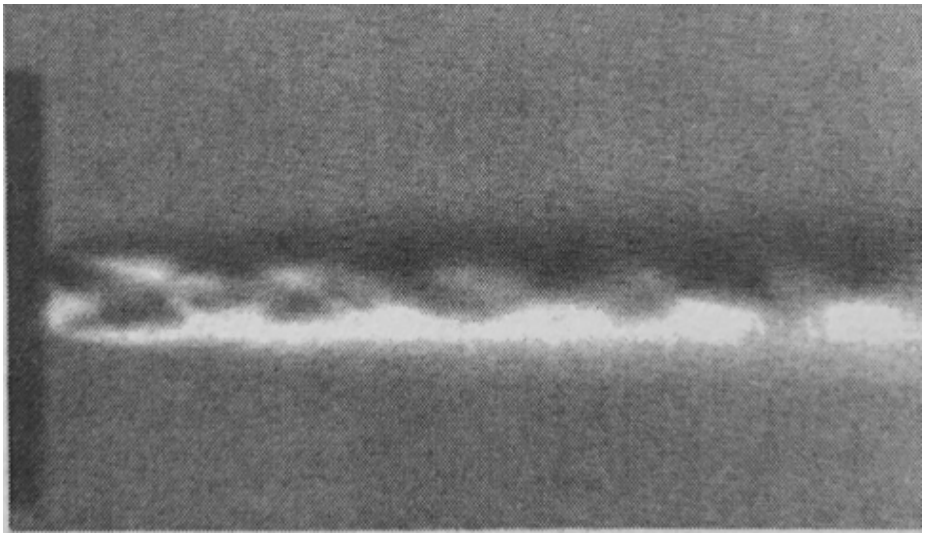

Figure 2.31: Nozzle exit Schlieren image [8]

In this thesis, Toepler′s Z-type Schlieren system was installed to visualize the flow field at the nozzle exit region with a jet vane. The BEM static fire test was performed at known boundary condition as mentioned in the numerical part of this section. In this test, pressure was measured also to understand whether the SRM is working well at design conditions, so the flow conditions are the same as numerical boundary conditions.

The Schlieren system was installed on the MATMS. This system consists of a light source (short-arc xenon lamp), two adjustable 10 inc parabolic mirror, a knife edge adjustable in all three axes, a plain mirror and a viewing screen (Figure 2.32).

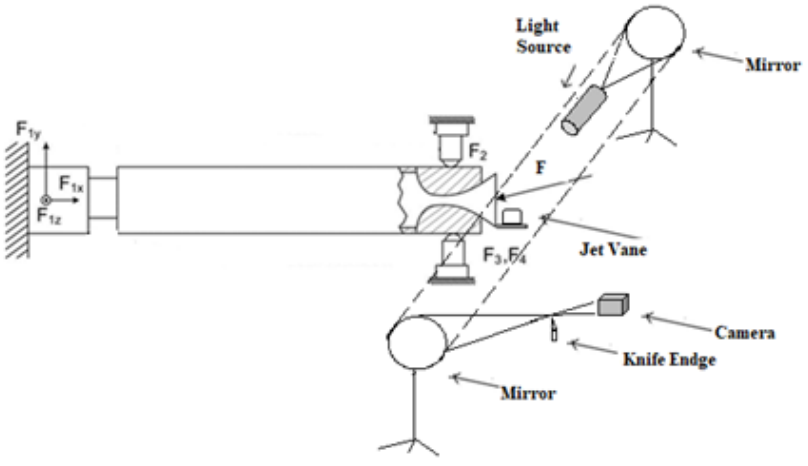

Figure 2.32: Z-type Schlieren layout drawing with MATMS

Figure 2.33: Schlieren layout on MAMTS

The Schlieren images were recorded with a high speed camera (Photron SA-X2) and an ordinary camera (JVC GC-PX 100BEU). High speed camera was connected to the data acquisition system for taking images synchronously at 5000 fps.

With the installed Schlieren setup, images were collected during static firing tests with the jet vane at 0°and 30° AoA. The obtained experimental Schlieren visuals are compared with the numerical analysis.

2.4 Analysis Methods

The experimental Schlieren imaging results used to describe the flow patterns over the jet vane in a quantitative manner as shown in Figure 2.34.

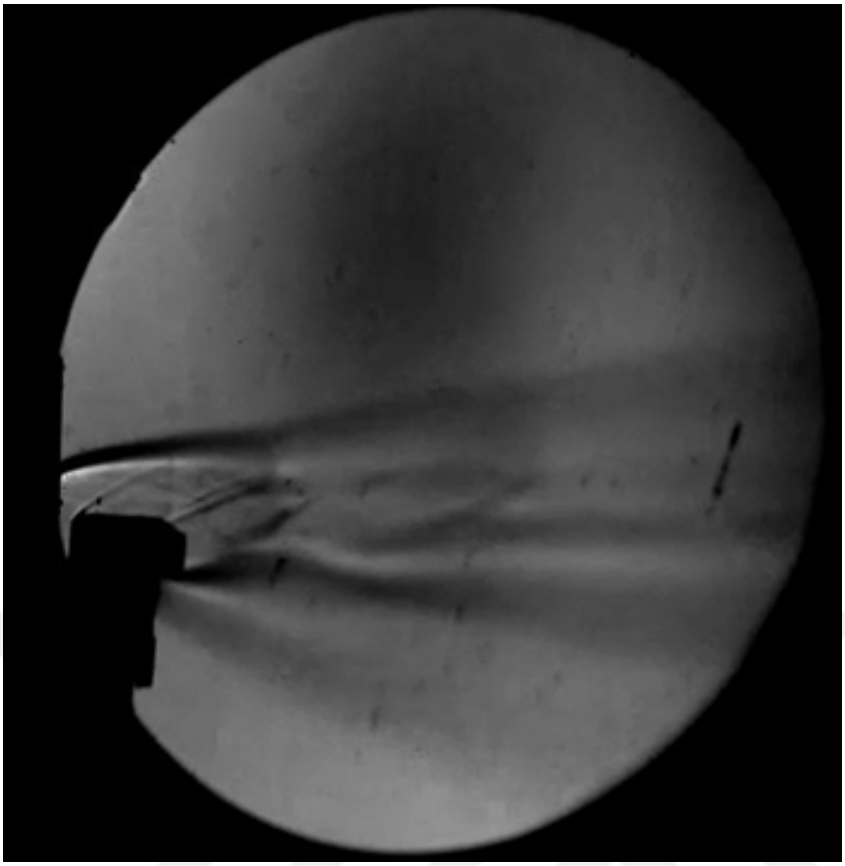

Figure 2.34: Schlieren visuals of BEM with jet vane static firing test

Numerical Schlieren pictures are generated for capturing shocks and expansion waves on a jet vane from the computed flow fields. The numerical Schlieren is defined from density gradient field at the jet vane section plane [32]. 2D section of jet vane lateral center is extracted from the numerical simulation and the density gradient is obtained in this plane as follows. Numerical and experimental Schlieren visuals around the jet vane are compared in Figure 2.35.

$$|\bigtriangledown\rho| = \sqrt{\left(\frac{\partial\rho}{\partial x}\right)^2 + \left(\frac{\partial\rho}{\partial y}\right)^2} \tag{2.3}$$

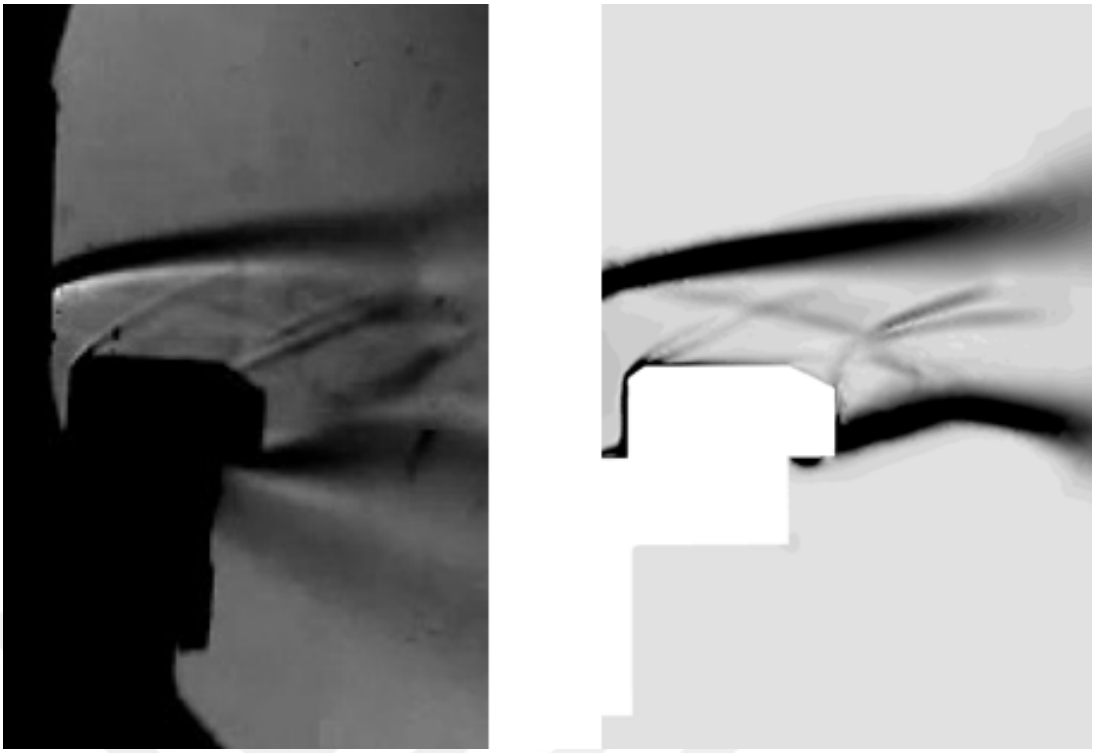

Figure 2.35: Comparison of (a) experimental and (b) numerical Schlieren visualization of the flow through jet vane

The Schlieren visualization studies were also carried out in order to investigate the supersonic flow on the SRM nozzle and the jet vane at 30 degrees AoA. The Z-type Schlieren technique is a two-dimensional flow visualization technique. It can visualize phenomena occurring in a two-dimensional section within the flow domain. Even though the Schlieren technique yields two-dimensional images, the resultant images are essentially superposition of several streamwise planes. To validate our numerical analysis with the Schlieren technique, we divided the flow volume around the vane into evenly spaced sections (see Figure 2.36) and superimposed the images in these sections (Figure 2.37). Thus, the three-dimensional effects of the flow around the deflected vane can be captured by numerical the Schlieren.

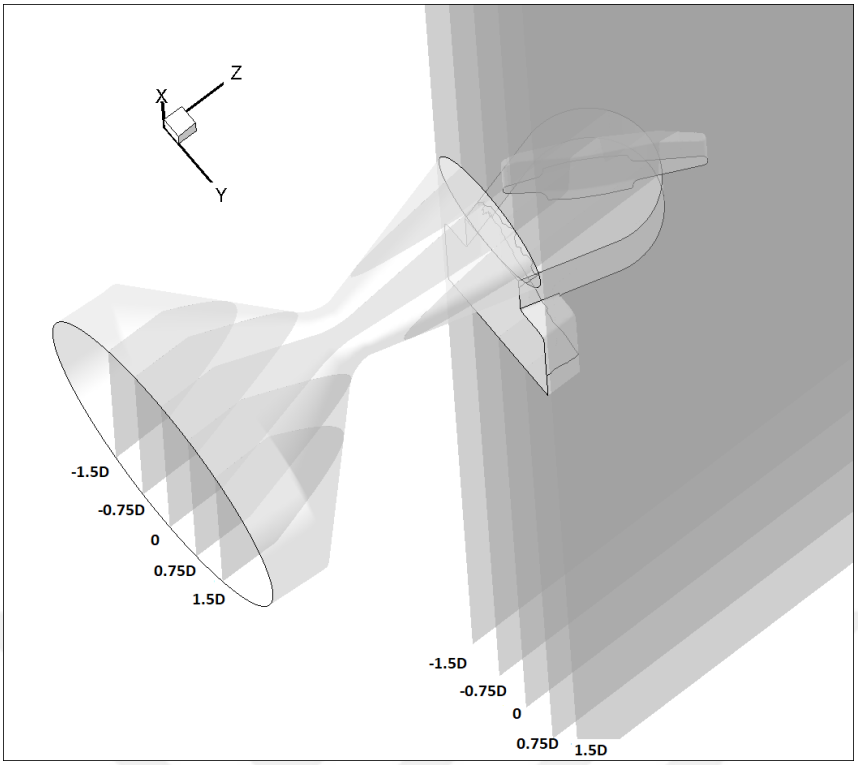

Figure 2.36: Flow domain near the vane obtained from numerical simulations is sliced into 5 planes

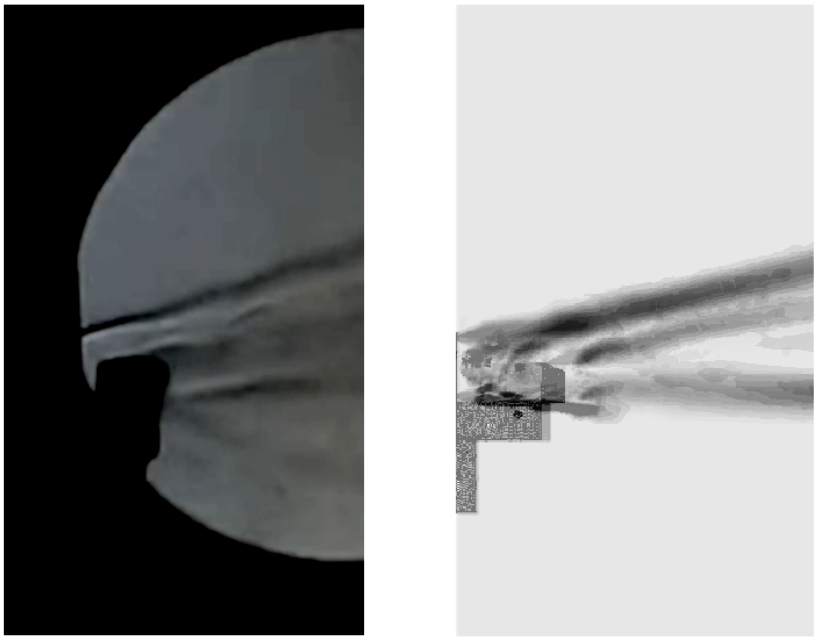

Figure 2.37: (a) experimental and (b) numerical Schlieren visualization of the flow through the jet vane at 30 degree AoA

CHAPTER 3

RESULTS AND DISCUSSIONS

In this thesis study, the flow topology around the jet vane is described and discussed in detail for different angles of attack. The prominent flow structures around the jet vane in the supersonic flow are investigated and fully three-dimensional numerical simulations were performed. The numerical results of these simulations are compared and verified with the results obtained from the static firing tests of the solid rocket motor-jet vane model. Special attention is given to the interaction between the hot exhaust gas and the jet vane. Schlieren visualization results are used to obtain the general flow patterns around the jet vane and subsequently to validate the numerical solver.

3.1 Flow Topology of a Jet Vane at 0° AoA

The jet vanes shape is identical to a supersonic wings shape. Both of them have a double wedge airfoil with an aspect ratio. Hence, supersonic wings can guide us to understand a jet vane′s characteristics. Theoretical study of a double wedge airfoil, numerical and experimental studies on a supersonic wing may help us understand the structures of the complex flow on a jet vane [23–25]. The Figure 3.1 illustrates the flow phenomena around a vane at the AoA of 0° in a supersonic flow.

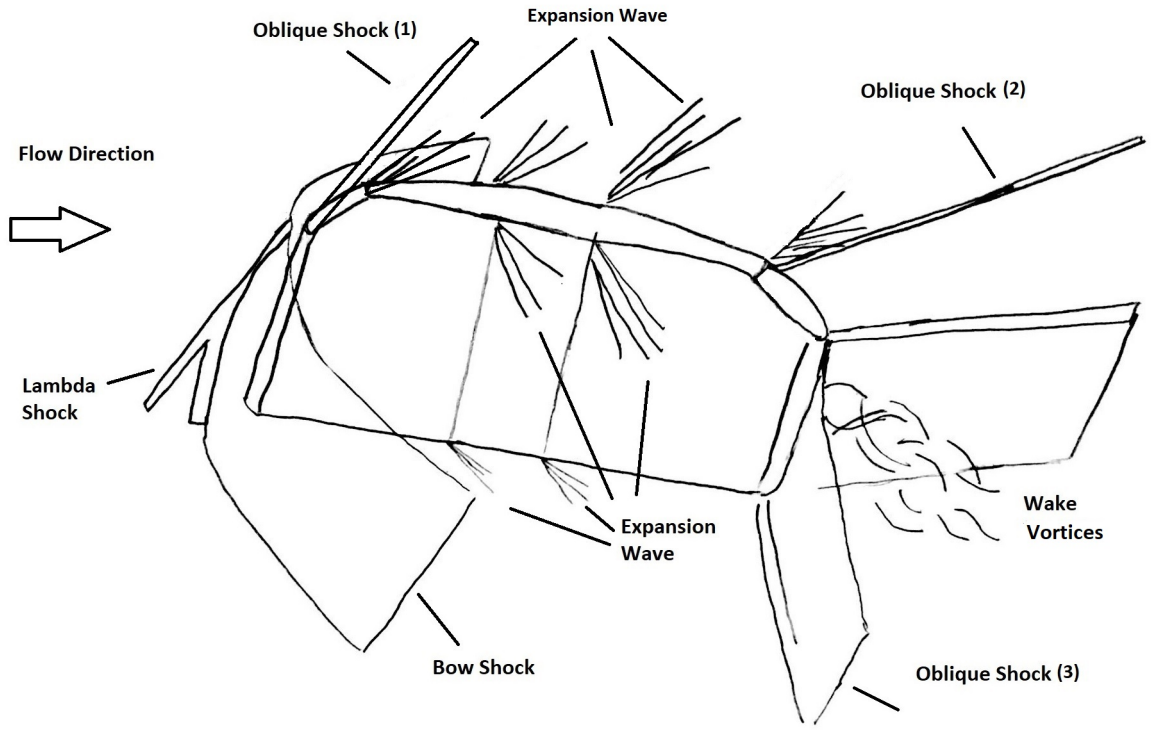

Figure 3.1: Schematic of 3-D flow physics around a generic jet vane

From the vane leading edge to the trailing edge: a very strong bow shock wave is established in front of the jet vane because the leading edge of the vane is rounded to reduce aerodynamic heating. A lambda shock occurs as a result of the separation of the boundary layer at the front of the bow shock. The strong bow shock wave ramifies near the flat plate on which the vane is placed. The tip of the leading edge creates a main oblique shock (Oblique Shock (1)) wave because of the concave corner surface. The flow decelerates through the oblique shock at the tip. After the oblique shock, the flow at the tip of the vane continues and encounters a convex surface. Then the flow at the vane tip expands and continues to the trailing edge. The flow expands across a series of expansion fans due to the flow encountering convex surfaces. On top and side surfaces along the vane, expansion waves are formed due to these convex geometrical shapes. Towards the back of the jet vane, the flow at the tip encounters a convex corner. The flow starts to expand at the corner and continues to expand through the surface. As a result of this expansion, the flow velocity increases such that an oblique shock (Oblique Shock (2)) wave is formed. On the side surfaces towards the rear part

of the vane, expansions take place and the oblique shock (Oblique Shock (3)) waves form at the trailing edge because of the concave edge effect. Then, there occurs a wake flow downstream of the vane.

The numerical (CFD-based) and experimental Schlieren results are compared incFigure 3.2). The flow around the vane which is placed at the exit of a nozzle differs from a single vane in a supersonic flow in the sense that there occurs an interaction between the vane and the supersonic exhaust gases.

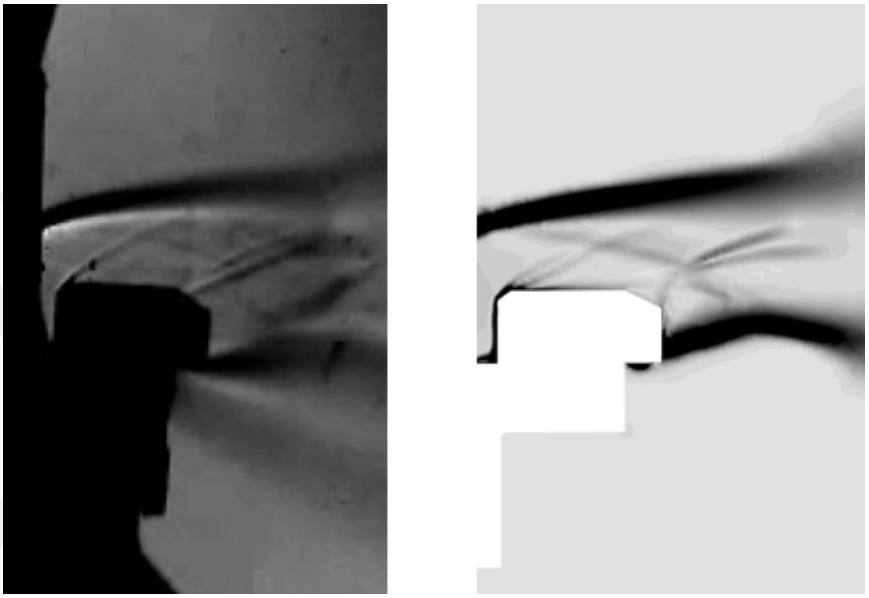

Figure 3.2: (a) Experimental and (b) numerical Schlieren visualization of the flow through the jet vane

Following the described numerical approach, the simulation was completed for the vane at zero angle of attack. The normalized Mach contours (Figure 3.3, 3.4) are plotted to study the interaction between the flow patterns of the jet vane and the hot exhaust gas flow.

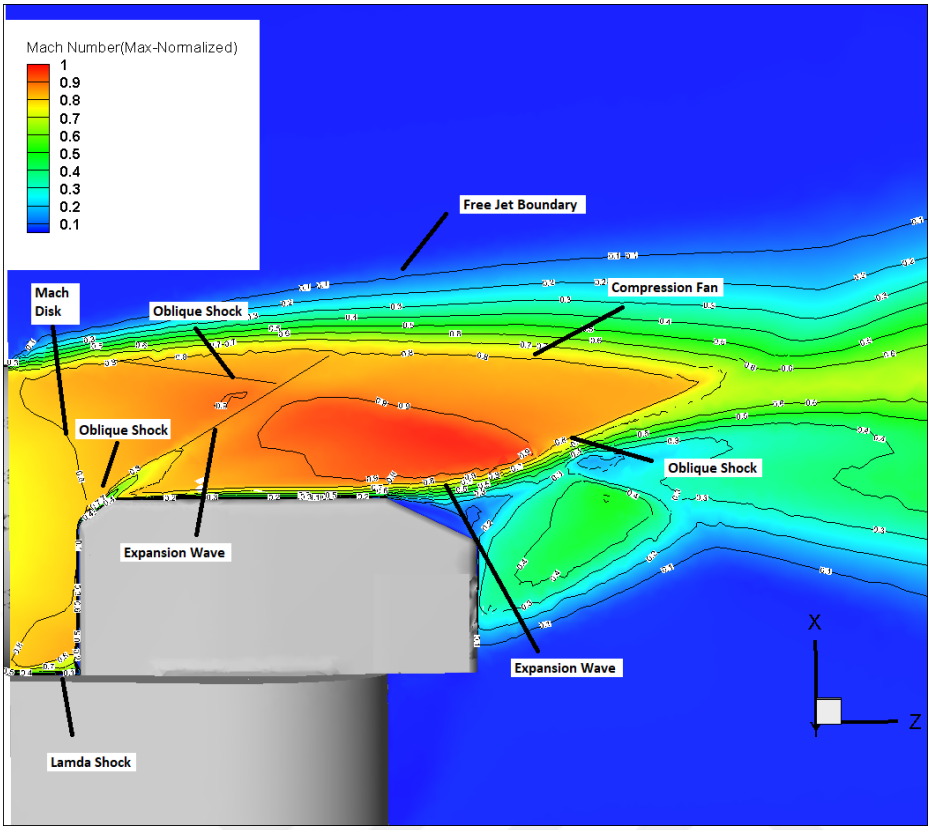

Figure 3.3: Normalized Mach contour-side view [0°− case]

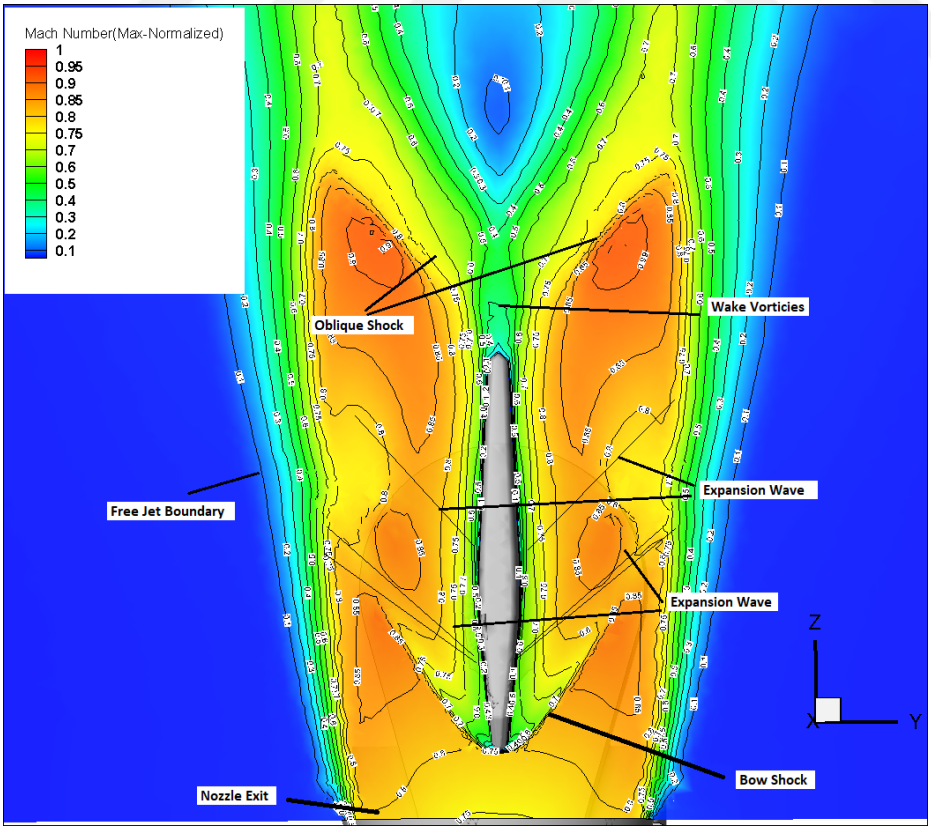

Figure 3.4: Normalized Mach contour-top view [0°− case]

As seen in the figures, the flow around the vane consists of a bow shock, the oblique shocks, the expansion waves and the wake vortices. Also, It is seen from the contours that a lambda shock occurs in the area where the vane is mounted on the base plane. In addition to the numerical simulation outputs and the Schlieren images which are shown before, the density gradient can easily be seen to created shocks and expansion waves. The similarity in shocks and expansions angles was observed with the Schlieren technique.

The numerical results are given in detail. Pressure distribution on the vane surface, the contours of total temperature, total pressure, Mach number of the cross-sectional plane of the solution domain and the vane at 0°angle of attack are presented (Figure 3.5 and 3.6). The lift and drag values which are obtained in the numerical simulations and in the experiments will also be presented.

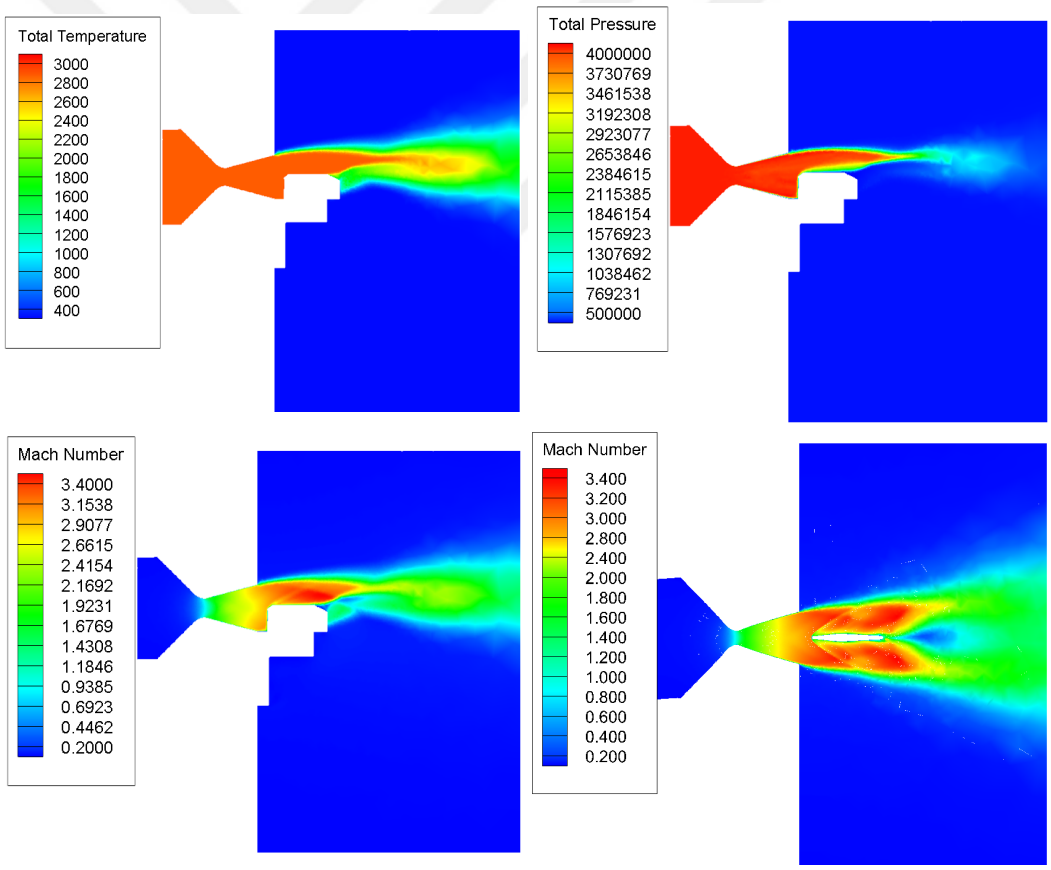

Figure 3.5: Total temperature (K), total pressure (Pa), Mach number-section view from side and , Mach number-section view from top at zero AoA

The computed surface pressure distribution on jet vanes for zero AoA is presented

(Figure 3.6). After the bow shock, the pressure distribution took form at the leading edge of the jet vane. The rounded corner changed the shock characteristic at the vane edge. The stagnation pressure occurred away from the surface of the vane. However, the pressure reaches its highest value at the leading edge of the vane. The pressure distribution on the vane surfaces changes according to the deflection. The absence of any deflection in the jet vane causes the pressure distributions on the upper and lower surfaces to be equal so that the jet vane can not produce lift. With this pressure distributions, only the drag force occurs.

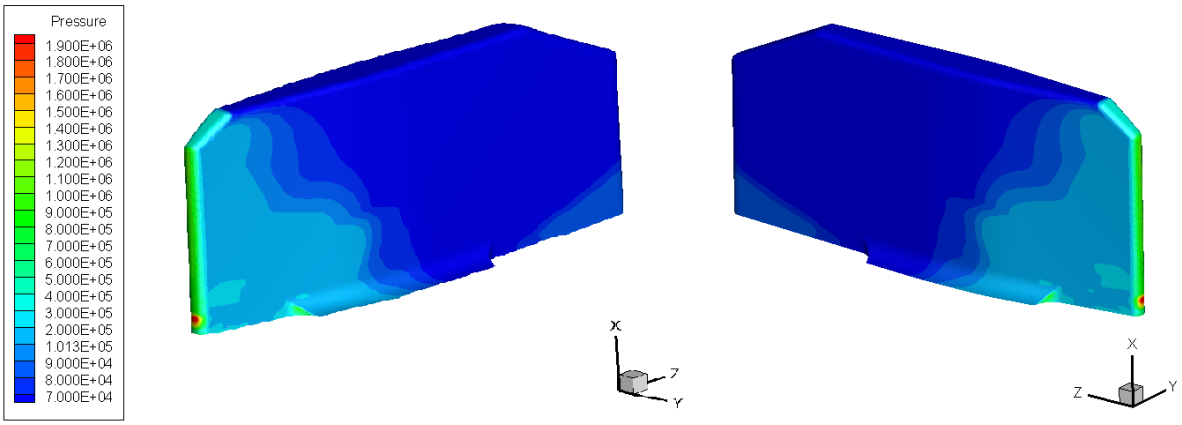

Figure 3.6: Surface pressure distribution at zero AoA

In the experimental part, tests were performed and test data were gathered with the mentioned sensors and data acquisition system. In Figure 3.20, a visual from static the SRM firing test.

Figure 3.7: Image from static firing test

Firstly, pressure measurements are essential for comparing theoretical calculations with the test case. The pressure value is used to assess the SRM performance. In addition, the pressure value obtained in the test case constitutes the boundary condition of numerical analysis. The pressure values obtained from tests give very close values to the theoretical value of which calculations done by NASA CEA. The lateral force values obtained from the force measurement system with the 3 load cells. Taking into account the geometry of these sensors standing at 120 degrees, the lateral force is calculated by using the load cells data (See Appendix A). The results of the pressure measurement and force measurements are given in Figure 3.8.

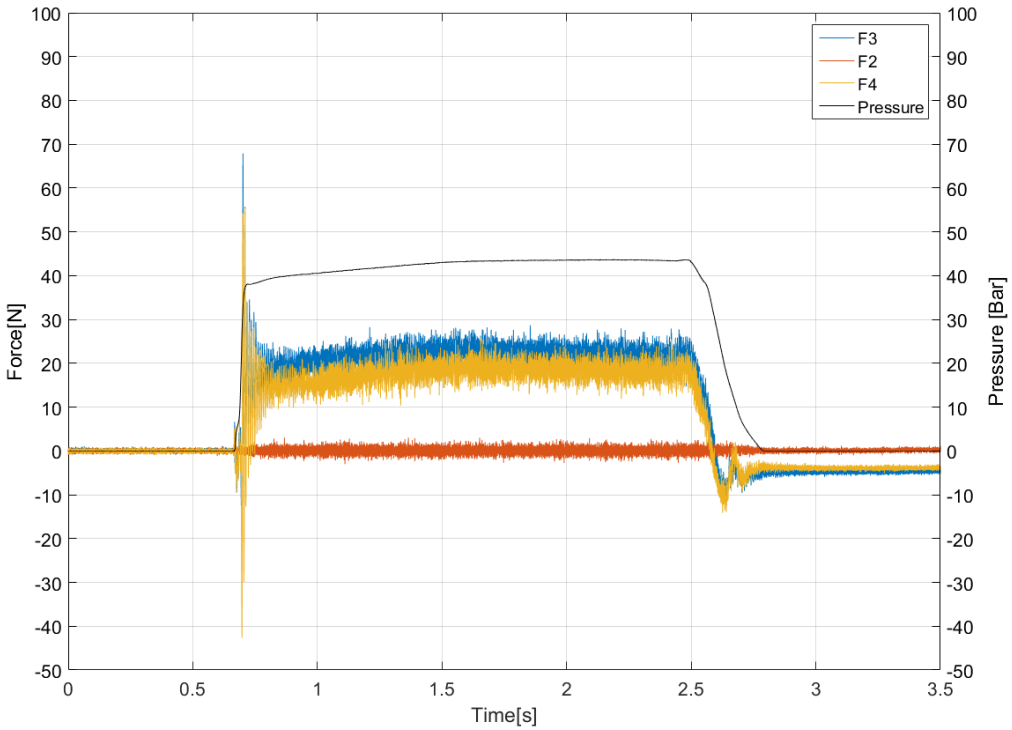

Figure 3.8: Measured pressure and load cells data for 0 degree. (F_2, F_3, F_4)

Images of the jet vane before and after the test, are given in Figure 3.9.No ablation occurred on the jet vane, so the forces only changed due to the pressure acted on it, yet the jet vane shape did not change.

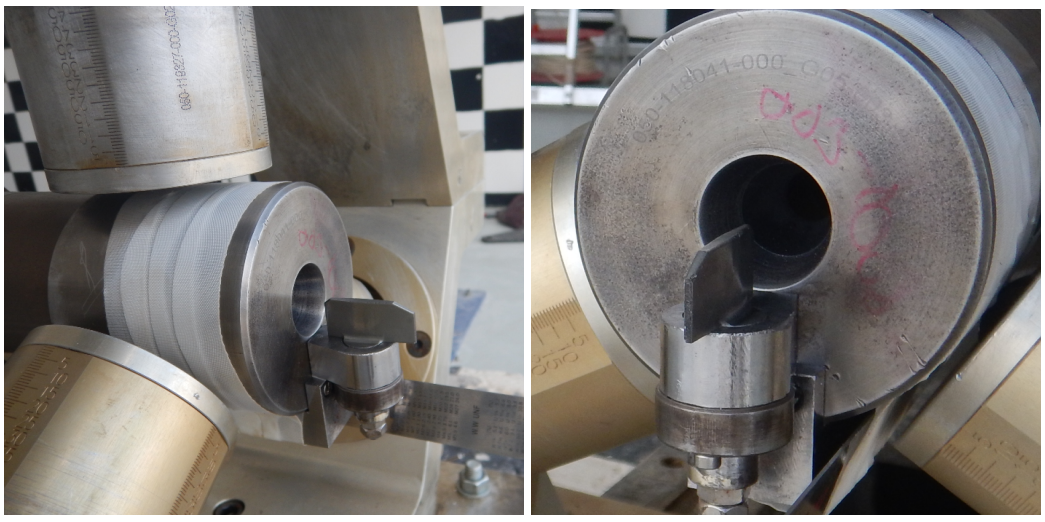

Figure 3.9: Jet vane view before and after static firing

The results are obtained from tests and analyses. % Differences between tests and

experiments are found with the given formula:

$$\%_{\text{error}} = \left| \frac{\text{Value}_{\text{experimental}} - \text{Value}_{\text{numerical}}}{\text{Value}_{\text{numerical}}} \right| \times 100 \tag{3.1}$$

Table 3.1: Comparison of experiment and numerical simulation results for the jet vane at zero degree AoA

	Numerical	**Experimental**	**% Differences**
Lift Force (N)	0	0	0
Drag Force (N)	17.754	17.38	2.151898734

3.2 Effect of AoA

3.2.1 Lift and Drag Generation

The jet vane generates aerodynamic forces analogous to the supersonic wing generating force at an angle of attack. The deflection in the jet vane changes the pressure distributions on the upper (suction side) and lower surfaces (pressure side). The pressure difference between the upper and lower sides of the vane creates a force normal to the chord of the jet vane. When the normal force is decomposed into force components, the force perpendicular to the flow direction corresponds to the lift (lateral force) and the component in the flow axis forms the drag.

3.2.2 Flow Fields

In this part, the numerical solution and test results of 10°, 20°and 30° jet vane angles are given in detail and the results of the numerical solutions and the measurements are compared.

Following the described numerical approach, the simulation was completed for the vane at 30 °angles of attack. The normalized Mach contours (Figure 3.10) are plotted to examine the interaction between the flow patterns of the jet vane and the hot exhaust gas flow.

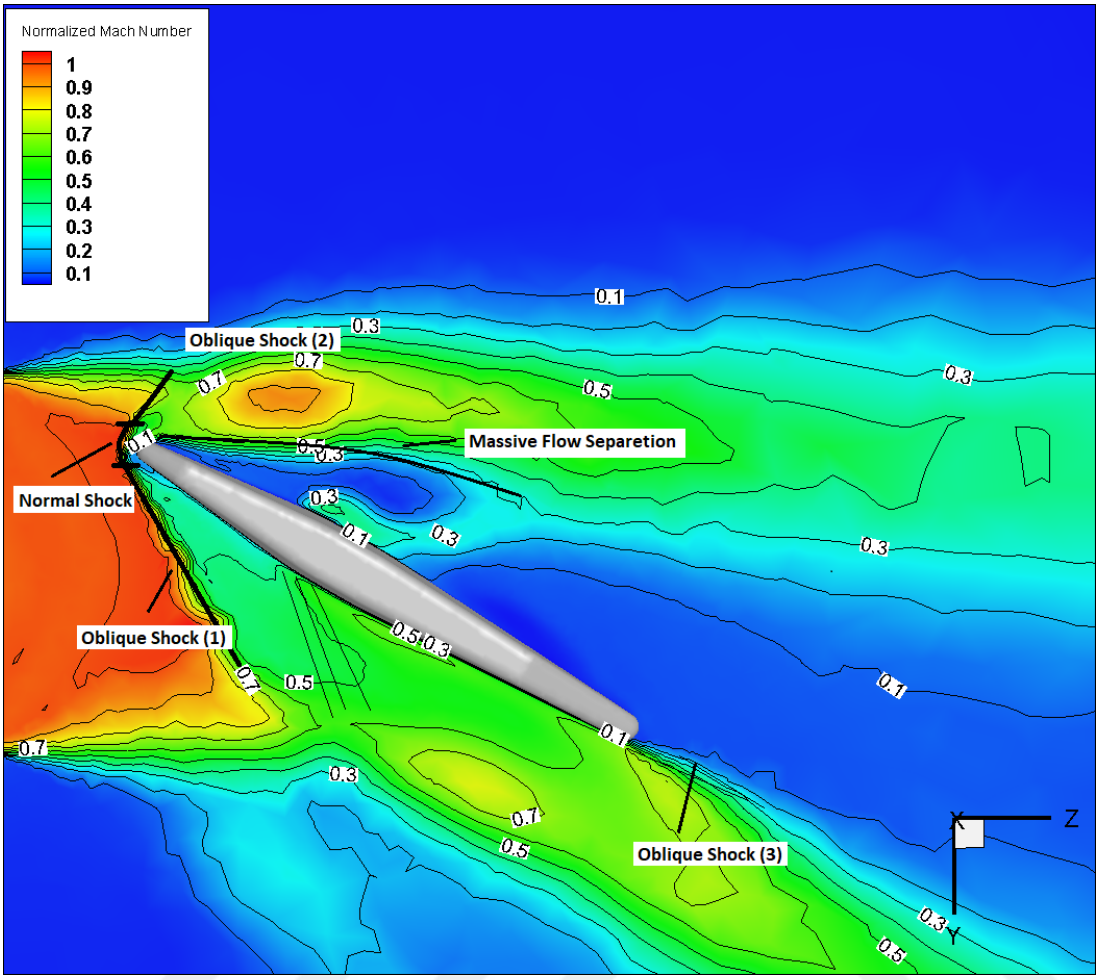

Figure 3.10: Normalized Mach contour of the jet vane at 30 degree AoA.

When the jet vane is deflected, a bow shock (detached shock) occurs at the head of the vane (Oblique Shock (1)+Oblique (2)+Normal Shock). At the blunt nose of the vane, the velocity decreased to subsonic speeds because of normal shock. An oblique shock forms at the pressure side of the vane and pressure increases at that side (Oblique Shock (1)). At the suction side, pressure decreases dramatically because of massive flow separation.

In the described numerical approach, the simulation was completed for the vane at 20 and 10 degree angles of attack. The normalized Mach contours (Figure 3.12 and 3.11) are also plotted to examine the interaction between the flow patterns of the jet vane and the hot exhaust gas flow.

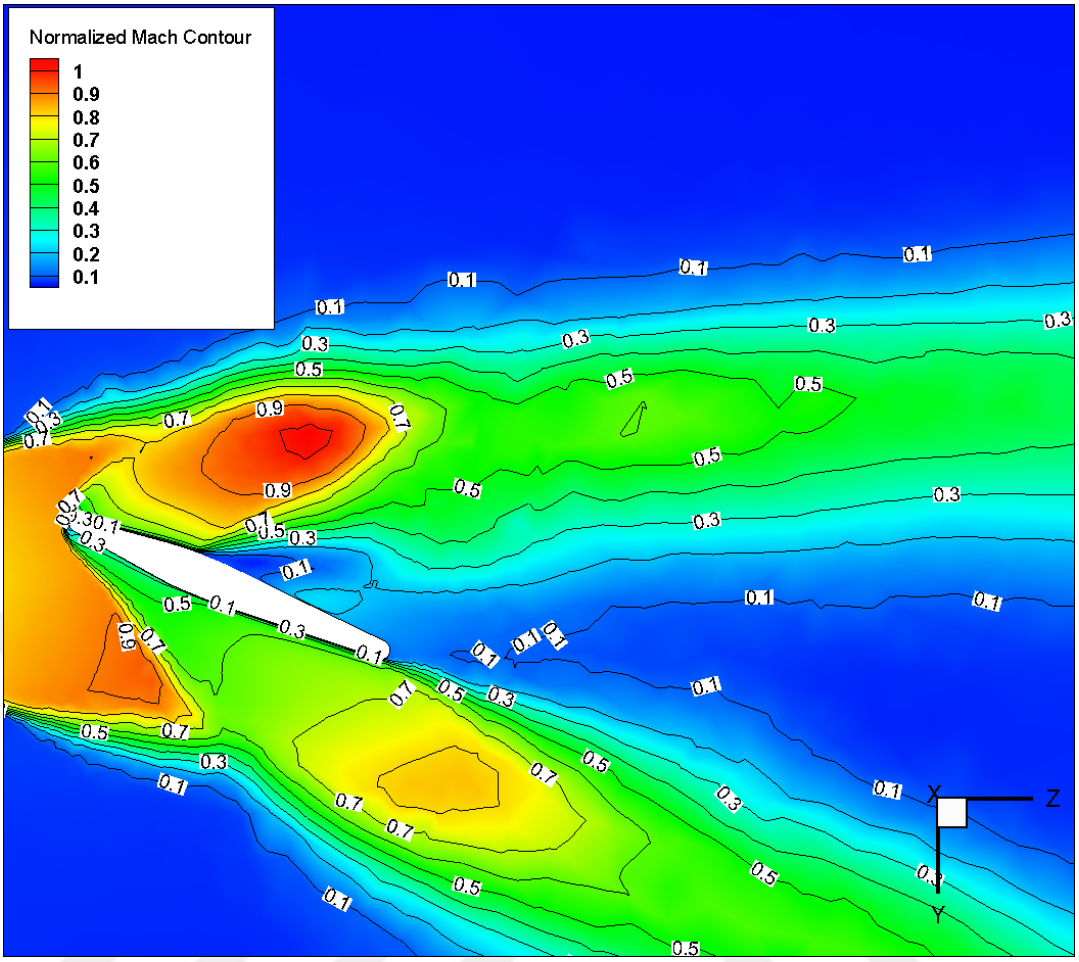

Figure 3.11: Normalized Mach contour of the jet vane at 20 degree AoA.

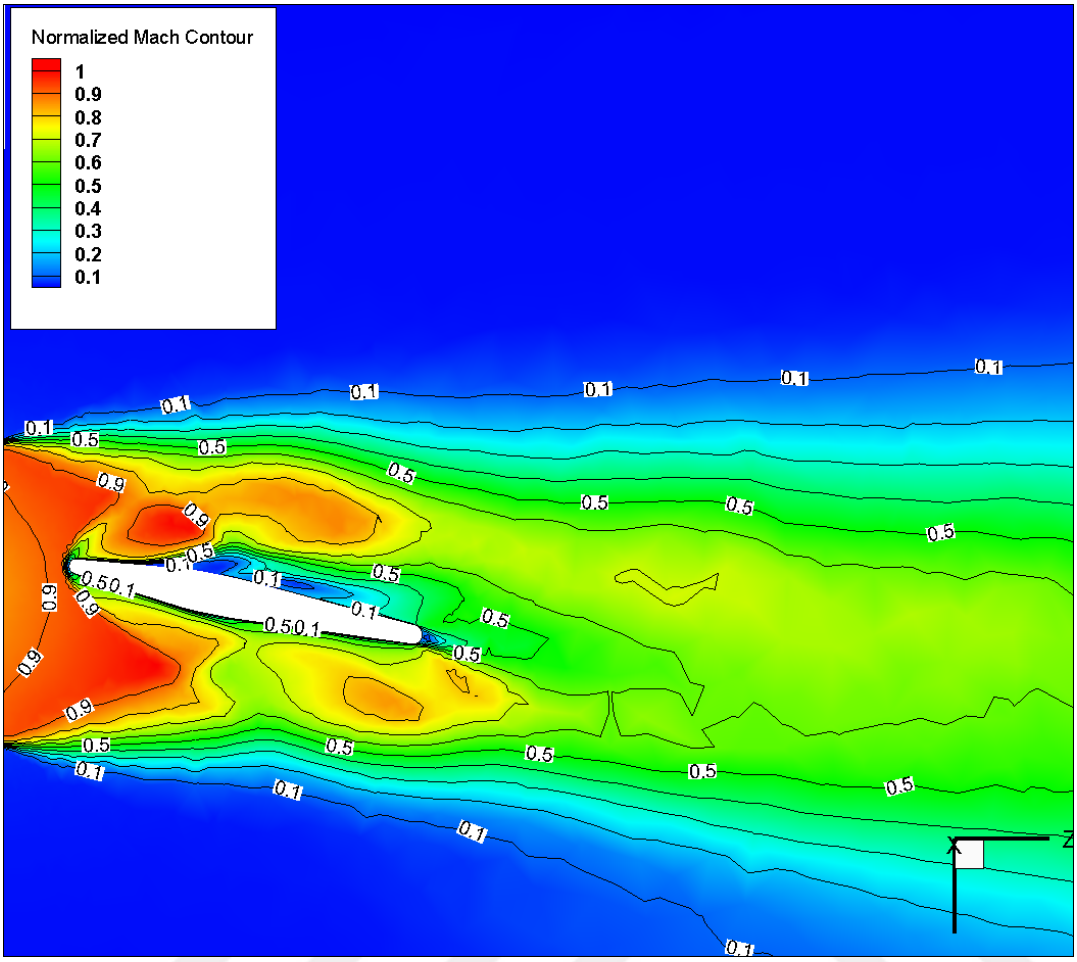

Figure 3.12: Normalized Mach contour of the jet vane at 10 degree AoA.

The values of pressure in the pressure side of the vane increase with a positive angle of attack and at the suction side surfaces, the shock weakens, eventually causing expansion at a higher angle of attack. In addition, with the increment of the angle of attack, the vortex becomes stronger and the vortex center moves toward the nose. However, with the effect of plume shocks at 20 degrees, the plume oblique shock interacts with the vane on the upper surface. Therefore, the vortex core did not move toward the nose.

The pressure distributions on the vane for 10, 20 and 30 degrees were obtained numerically (Figure 3.13).

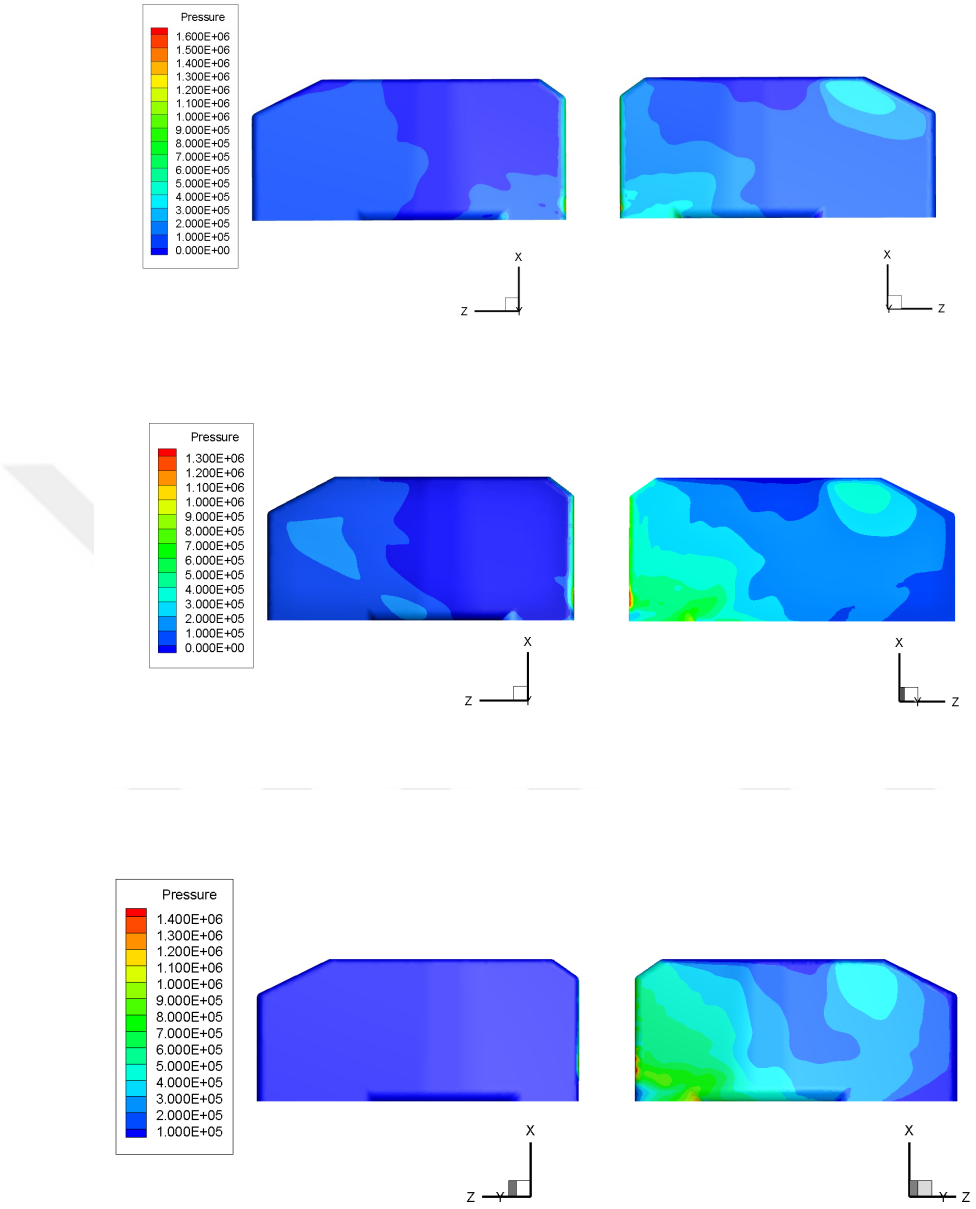

Figure 3.13: Pressure distribution of the jet vane - from top to bottom 10, 20 and 30 degree (Upper Surface-Left, Lower Surface-Right)

Shock and expansion waves on the jet vane and plume-jet vane interaction were captured with numerical Schlieren approach. As a result, it can be said that the numerical Schlieren was validating our CFD solver, mesh structure and endmost our force values.

The equally spaced sections were examined separately for the 3D case. The sections are named as -1.5D, -0.75D, 0, 0.75D and 1.5D (Figure 3.14). The section 0is located in the middle of the solution domain. Sections -0.75D and 0.75D are placed at equal distances from the center (section 0). Section -1.5D and 1.5D are also placed at an equal distance from the center. Sections -1.5D and -0.75D are placed at the upper surface side of the vane and sections 0.75D and 1.5D are placed at the lower side of the vane.

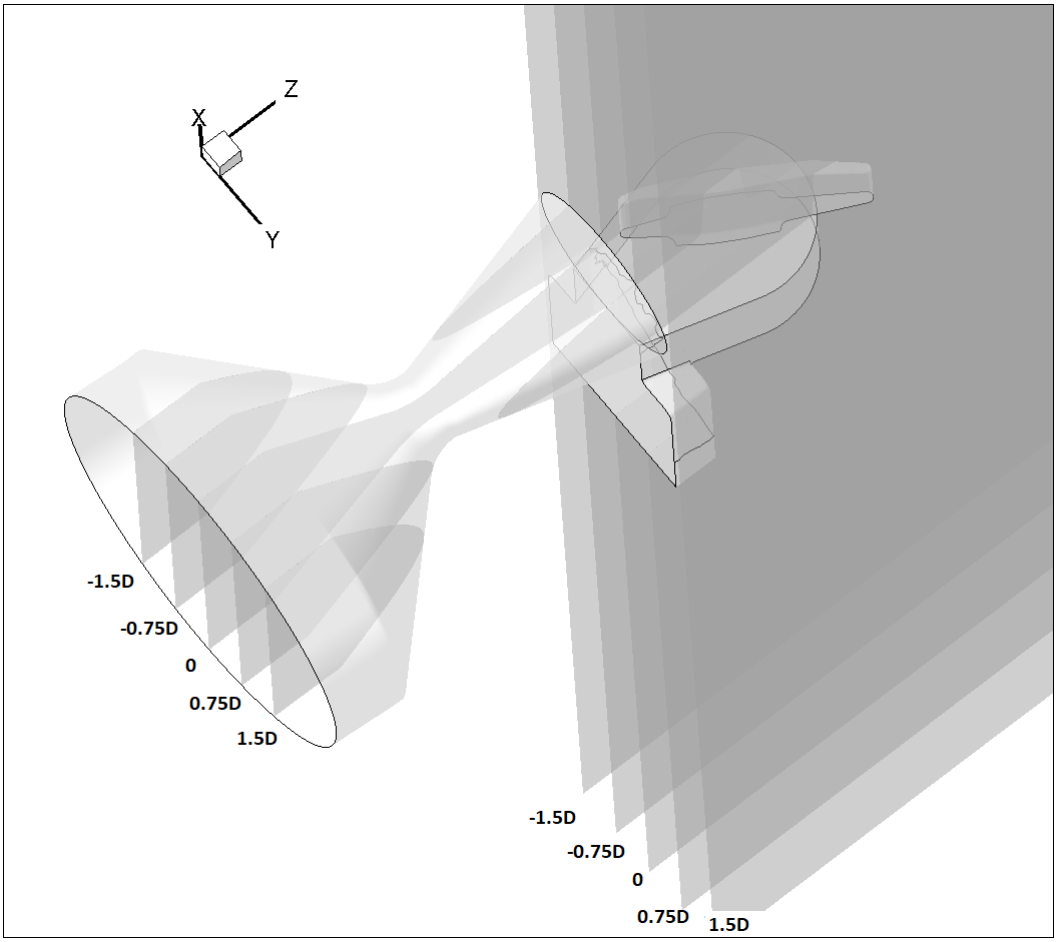

Figure 3.14: Flow domain near the vane is sliced into 5 planes

Section -1.5D is located at a small distance away from the leading edge of the vane. In this section, the jet vane-plume interaction is not observed. Section -0.75D shows the phenomena that occur at the tip of the vane. A lambda shock on the vane tip and oblique shock on the concave surface of the wing are seen in section -0.75D. Furthermore, the compression waves from the plume and the oblique shock are intricate. In the image taken from the section 0, the bow shock and the boundary layer of the jet

vane adaptor interact at the lower side of the vane. As a result of this interaction, a lambda shock occurrs. In addition, it is also observed in this section that the strong bow shock placed in front of the vane deflects the nozzle plume. The oblique shock on the concave surface at the trailing edge of the vane is clearly visible in the section 0.75D. Also, the formation of wake vortices behind the vane are observed in this section. In section 1.5D, it is seen that the oblique shock formed at the trailing edge of the vane is weakened in the plume and continued downstream. The result of the plume interaction with the jet vane adaptor, an oblique shock is placed at the edge of the adaptor. Furthermore, wake vortices on the vane trailing edge are observed in this section (Figure 3.15).

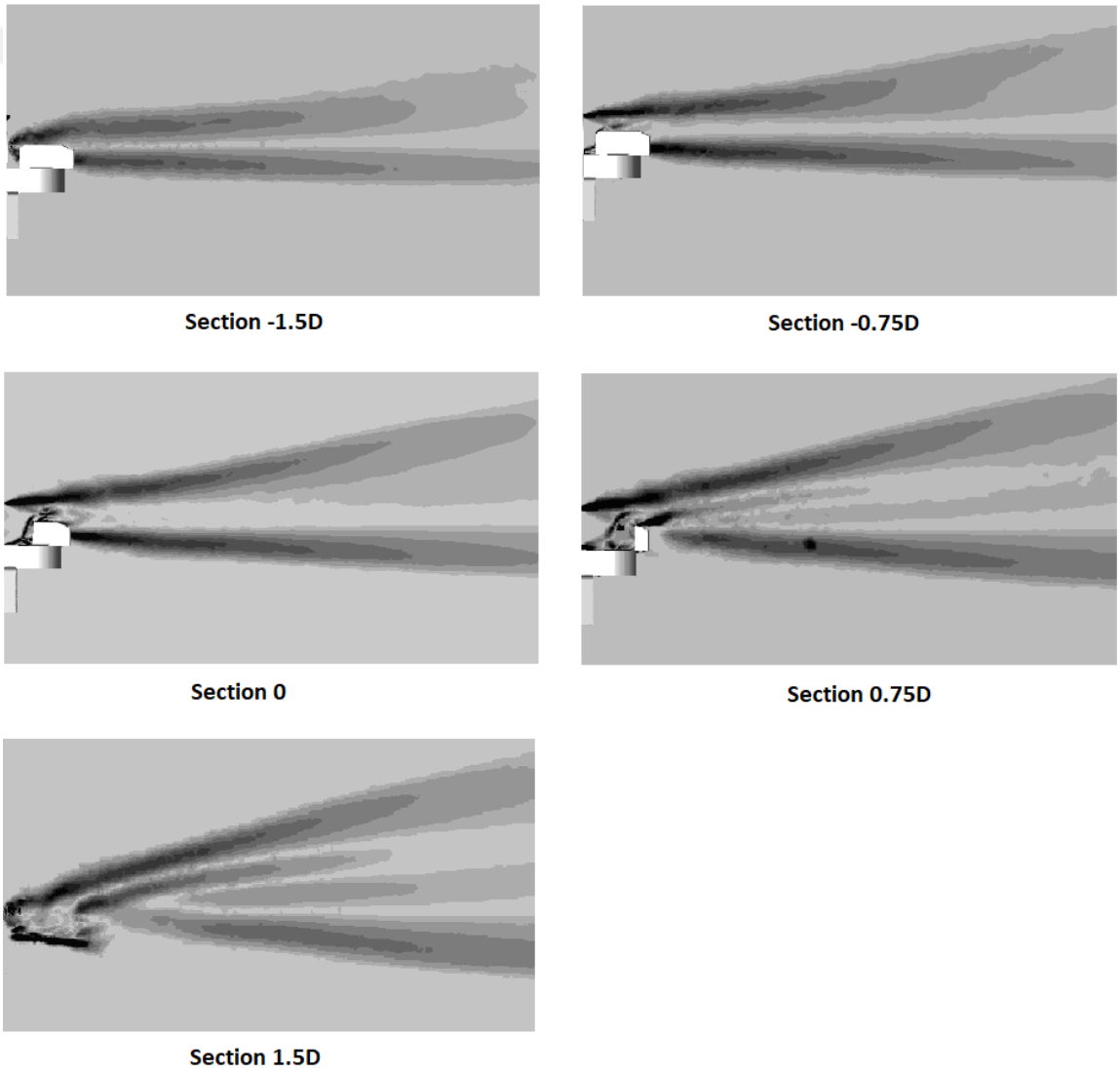

Figure 3.15: Visual of sections obtained from the numerical solution domain for 30° AoA

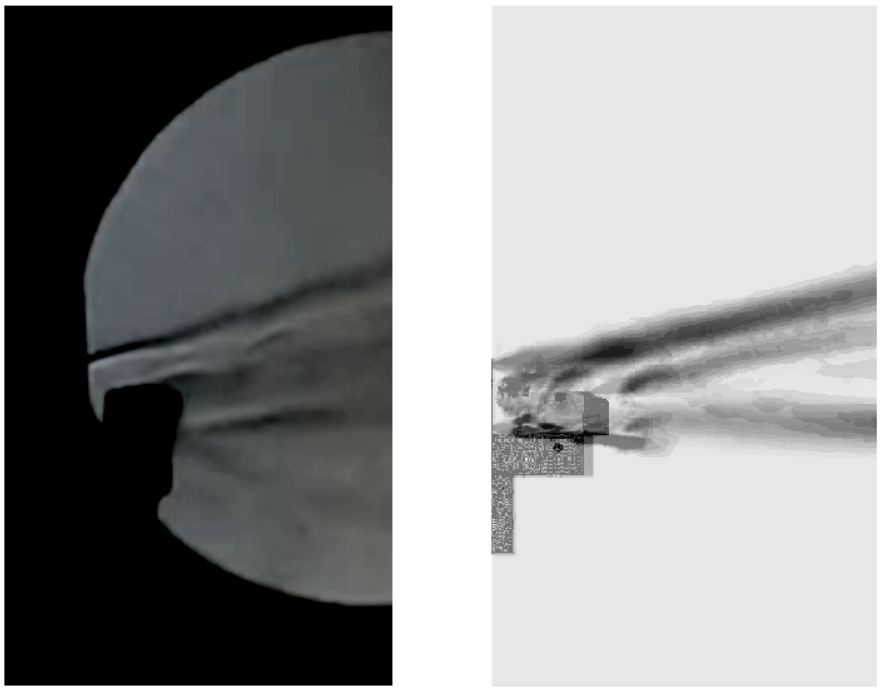

Figure 3.16: (a) Experimental and (b) numerical Schlieren visualization of the flow through the jet vane at 30 degree AoA

The Schlieren system did not capture shock and expansion waves sharply. The interaction of the jet plume and separated flow on the vane was clearly demonstrated. The forces generated by the vane were found with the numerical analysis and given in the Table 3.3:

Table 3.2: Numerical simulation results for 0°, 10°, 20°, 30° AoA cases

	Numerical Simulation	
AoA (Deg.)	**Lift (N)**	**Drag (N)**
0	0	17.754
10	49.72	20.287
20	112.4	46.83
30	138.8	60.7

In this study, the effect of the vane on the inner flow of the nozzle is also examined. In Figure 3.17, 3.18 and 3.19, the top view of the Mach contours plot are given. The fact that the vane is sufficiently far from the nozzle outlet ensures that no shock wave enters into the nozzle. Furthermore, the presence of the vane is not large enough to increase the outlet pressure and create a blocking effect in the nozzle diverging part.

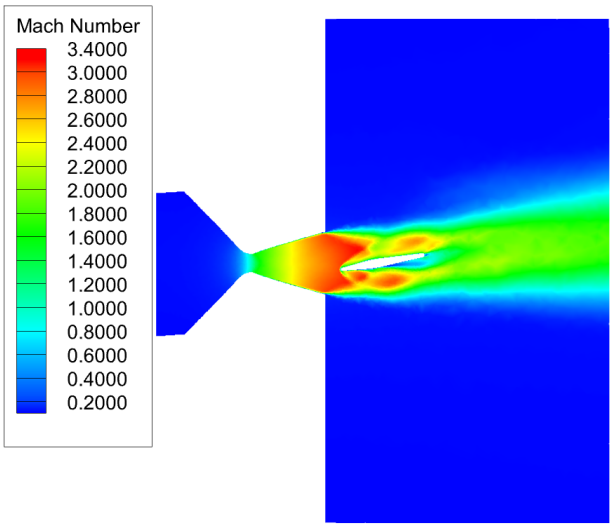

Figure 3.17: Top views of the Mach contour for the jet vane at 10 degree AoA

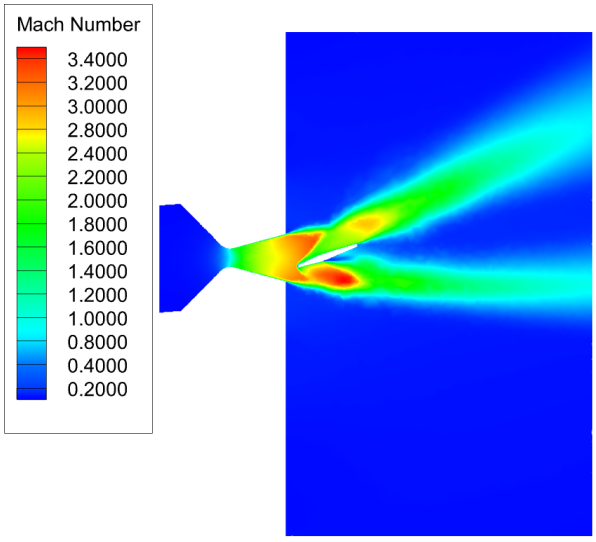

Figure 3.18: Top views of the Mach contour for the jet vane at 20 degree AoA

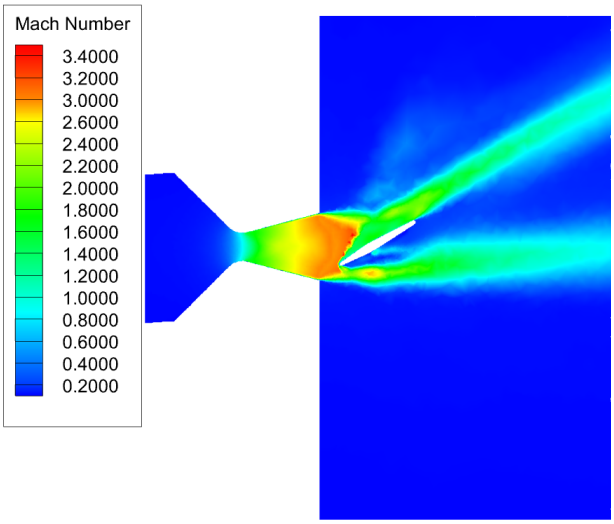

Figure 3.19: Top views of the Mach contour for the jet vane at 30 degree AoA

In the experimental part, the tests were performed and test data were gathered. An image which was captured during the static firing test at 20 degrees AoA is shown in Figure 3.20.

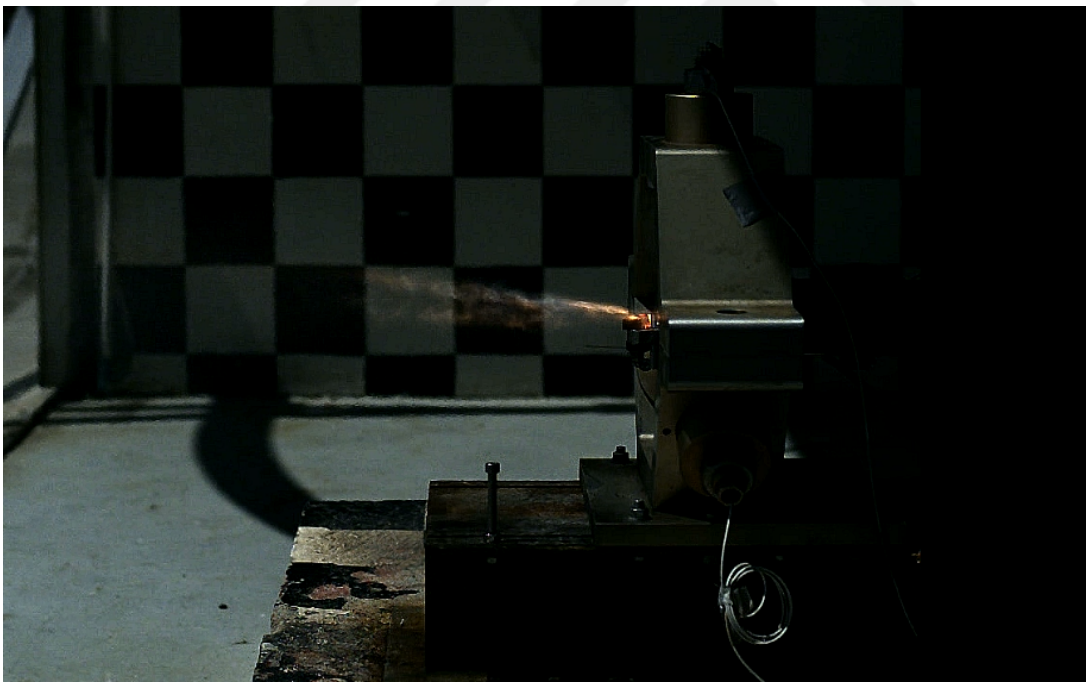

Figure 3.20: A visual during a static firing test - 20° AoA

Area of the jet vane surfaces did not change in the tests so that the control forces that are created by the vane were constant under the same surface pressure during the test. In Figure 3.21, the SRM-JVs images before and after static firing tests.

Figure 3.21: The SRM-JV assembly before and after tests

Firstly, the pressure data are important for comparing theoretical calculations with the test cases for different AoA. The lateral force values obtained from the measurement system with the 3 load cell. The drag of the jet vane at 10, 20 and 30 degree angles were calculated as a loss of axial thrust (Figure 3.22).

The axial force of the nozzle without vane mounted and the axial force obtained from the vane mounted tests at different angles are given in the graph (Figure 3.22). Drag force is increased with an increasing jet vane angle. This is seen in the graphs as a loss of axial thrust. In short, this is the drag force created by the jet vane.

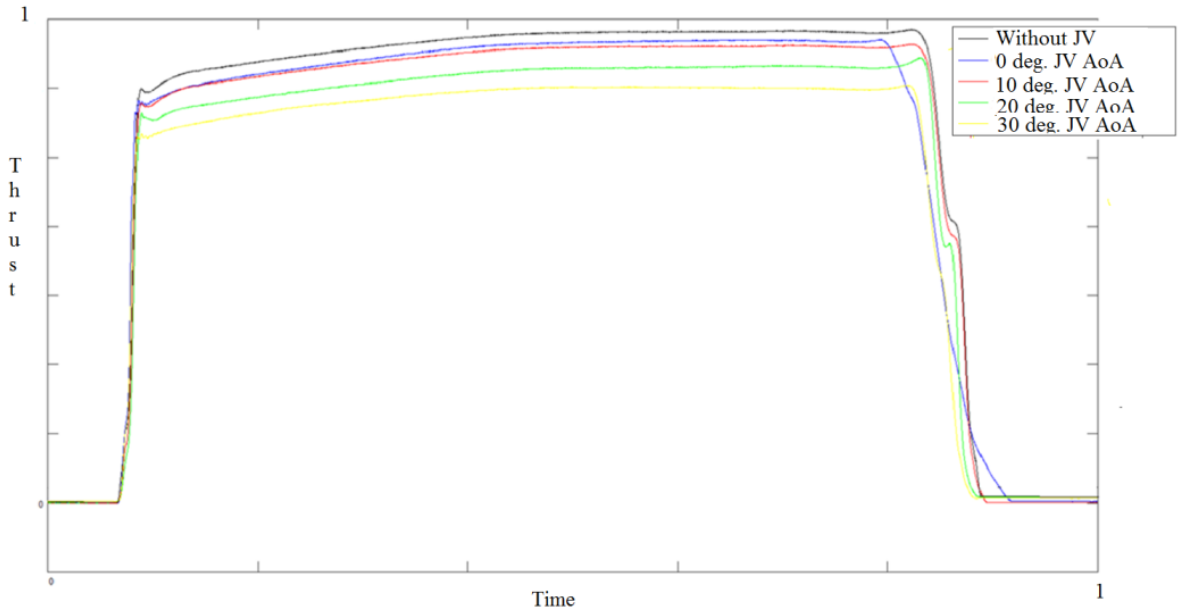

Figure 3.22: Thrust curves [0°, 10°, 20°, 30°– cases]

The lift and drag of the jet vane obtained from the tests and the numerical simulations are given in Table 3.3.

Table 3.3: Comparison of the experimental and numerical simulation results for four AoAs

	Numerical		**Experimental**		**% Difference**	
AoA (Deg.)	**Lift (N)**	**Drag (N)**	**Lift (N)**	**Drag (N)**	**Lift**	**Drag**
0	0	17.754	0.234	17.38	0.234	2.1519
10	49.72	20.287	50.64	21.13	1.81675	3.98959
20	112.4	46.83	121.4	50.25	7.41351	6.80597
30	138.8	60.7	151	65.33	8.01325	7.0871

It has been observed that the pressure difference between the surfaces of the vane increases with the increase of the angle, and consequently, the lift increases. The lift changes linearly up to 20 degrees and the increase are not linear due to massive separation at 30 degrees.

CHAPTER 4

CONCLUSION

The interaction between hot exhaust gas and the jet vane has been studied in detail and the results of numerical analysis and SRM-JV tests are given. Initially, the working environment of the jet vane is defined to reveal a numerical analysis model. The solution domain and mesh models are established by examining the working environments of the jet vane. In order to better understand the flow physics around the vane, the appropriate turbulence model and a wall function are studied. With the selected models, the shock characteristics around the vane are examined in detail in order to obtain the vane aerodynamic performance accurately. Regarding the flow physics, a very strong bow shock wave is established in front of the jet vane and a lambda shock occurs as a result of the separation of the boundary layer at the front of the bow shock. The tip of the leading edge creates a main oblique shock wave because of the concave corner surface and after the oblique shock, the flow at the vane tip expands and continues to the trailing edge. The flow expands across a series of expansion fans due to the flow encountering convex surfaces. All these phenomena have a direct effect on the forces generated by the vane by changing the pressure distribution on the vane. In addition, shock plume interactions and the effect of the vane on the inner flow of the nozzle are examined with the numerical analysis model.

The computational results are compared and verified with the results obtained from the static fire tests of the rocket motor and jet vane model. The experimental Schlieren imaging results are also considered to qualitatively utilize the flow over the jet vane so that numerical analysis is verified with the Schlieren technique. The experimental Schlieren imaging results are considered to utilize the flow over the jet vane qualitatively and the numerical Schlieren is defined as a density gradient magnitude at

the jet vane section plane. 2D section of the jet vane lateral center is taken from the simulation and the density gradient is shown from this plane. Capturing shocks and expansion waves on jet vane with the numerical Schlieren is validating our CFD solver, mesh structure and the calculated force values. Comparison of the test results and numerical results give approximately 8% amount of error at maximum AoA. All the investigations revealed that the numerical analysis approach is demonstrated the jet vane aerodynamic characteristics successfully.

For future work;

- More precise turbulence modeling should be used to capture the physical phenomenon better. Detached Eddy Simulation (DES) or Large Eddy Simulation (LES) can be used accurately to resolve the time evolution of flow around the jet vane with the internal flow field of the nozzle.

- The CFD study can be extended to model chemical ablation for different refactor material that jet vane is made. The transient analysis coupled with erosion model can be used to determine the geometry change due to ablation at the leading edge of the vane. The ablation characteristics can be found and pressure distribution on the jet vane can be captured accurately.

REFERENCES

[1] H. Mark, *Encyclopedia of Space Science and Technology*. Encyclopedia of Space Science & Technology, Wiley, 2003.

[2] E. Wong, "Design, fabrication and test of omnidirectional flexible seals for thrust vector control of large solid rocket motors," tech. rep., NASA, July 1971.

[3] H. Ko and W. S. Yoon, "Performance analysis of secondary gas injection into a conical rocket nozzle," *Journal of Propulsion and Power*, vol. 18, 05 2002.

[4] A. B. Facciano, K. G. Sybold, T. L. Westberry-Kutz, and D. O. Widmer, "Jet vane control system prototype hardware development for the evolved seasparrow missile," *Journal of Spacecraft and Rockets*, vol. 39, p. 26, 07 2002.

[5] V. Harrisson, A. Dechamplain, D. Kretschmer, R. Farinaccio, and R. Stowe, "Force measurements evaluating erosion effects on jet vanes thrust vector control system," 07 2003.

[6] A. L. S. 150, *Design Methods in Solid Rocket Motors*. No Atlantic Organization.

[7] A. Ünal, K. Yaman, E. Okur, and M. Adli, "Design and implementation of a thrust vector control (tvc) test system," *Journal of Polytechnic*, 03 2018.

[8] H. Reichenbach, "Contributions of ernst mach to fluid mechanics," *Annual Review of Fluid Mechanics*, vol. 15, pp. 1–29, 11 2003.

[9] G. Sutton and O. Biblarz, *Rocket Propulsion Elements*. A Wiley Interscience publication, Wiley, 2001.

[10] G. Jensen and D. Netzer, *Tactical Missile Propulsion*. Progress in astronautics and aeronautics, American Institute of Aeronautics and Astronautics, Inc., 1996.

[11] "Solid rocket thrust vector control," tech. rep., NASA Space Vehicle Design Criteria, December 1974.

[12] A. Davenas, *Solid Rocket Propulsion Technology*. Elsevier Science & Technology Books, 1993.

[13] M. F. Gomes, *Internal Ballistics Simulation of a Solid Propellant Rocket Motor*. PhD thesis, UNIVERSIDADE DA BEIRA INTERIOR, The address of the publisher, 7 2013. An optional note.

[14] C. Murthy and D. Chakraborty, "Numerical characterisation of jet-vane based thrust vector control systems," *Defence Science Journal*, vol. 65, pp. 261–264, 07 2015.

[15] P. GIRAGOSIAN, "Theoretical and experimental aerodynamic correlation of jet vane control effectiveness," *7th Atmospheric Flight Mechanics Conference*, vol. 7, 8 1981.

[16] R. Roger, S. Chan, and J. Hunley, "Cfd analysis for the lift and drag on a fin/-mount used as a jet vane tvc for boost control," 33rd Aerospace Science Meeting Exhibit, American Institute of Aeronautics and Astronautics, 1996.

[17] P.-A. Rainville, A. Dechamplain, D. Kretschmer, R. Farinaccio, and R. Stowe, "Unsteady cfd calculation for validation of a multi-vane thrust vector control system," 07 2004.

[18] Z. Stefanovi, M. Milos, I. Todic, and M. Pavlovi, "Investigation of the pressure distribution in a 2d rocket nozzle with a mechanical system for thrust vector control (tvc)," vol. 53, pp. 287–292, 07 2011.

[19] Y. Lee, S. Park, H. Chang, and Y. Cho, "Dynamic characteristics of the thrust vectoring control by highly compressible coanda effects," *29th Congress of the International Council of the Aeronautical Sciences, ICAS 2014*, 01 2014.

[20] V. Zmijanovic, L. Leger, E. Depussay, M. Sellam, and A. Chpoun, "Experimentalnumerical parametric investigation of a rocket nozzle secondary injection thrust vectoring," *Journal of Propulsion and Power*, vol. 32, pp. 196–213, 01 2016.

[21] J. Phillip, S. Youngblood, M. Grubelich, W. V. Saul, and M. Hargather, "Development and testing of a nitrous-oxide/ethanol bi-propellant rocket engine," 07 2016.

[22] A. Neely, F. Gesto, and J. Young, *Performance Studies of Shock Vector Control Fluidic Thrust Vectoring*, vol. 1. 07 2007.

[23] A. Shapiro, *The dynamics and thermodynamics of compressible fluid flow*. No. 1. c. in The Dynamics and Thermodynamics of Compressible Fluid Flow, Ronald Press Co., 1953.

[24] P. Sturdza, "Extensive supersonic natural laminar flow on the aerion business jet," vol. 12, 01 2007.

[25] P. R. Viswanath, "Shock-wave-turbulent-boundary-layer interaction and its control: A survey of recent developments," *Sadhana*, vol. 12, pp. 45–104, Feb 1988.

[26] M. Yu, J. Bae, H. H. Cho, and K.-Y. Hwang, "Hybrid method for jet vane thermal analysis in supersonic nozzle flow," *Journal of Thermophysics and Heat Transfer - J THERMOPHYS HEAT TRANSFER*, vol. 20, pp. 614–617, 07 2006.

[27] H.-G. Sung, "Thrust-vector characteristics of jet vanes arranged in x-formation within a shroud," *Journal of Propulsion and Power - J PROPULSION POWER*, vol. 20, pp. 501–508, 05 2004.

[28] M. LAUZON, *5DOF dynamic loads on a jet vane*.

[29] Ansys., "Reynolds averaged navier-stokes (rans) turbulence model," tech. rep., 2015.

[30] G. Settles, *Schlieren and Shadowgraph Techniques: Visualizing Phenomena in Transparent Media*. Engineering online library, Springer Berlin Heidelberg, 2001.

[31] D. W. Holder and R. J. North, "Schlieren methods," *National Physical Laboratory Notes on Applied Science*, no. 31, 1963.

[32] A. Hadjadj and A. Kudryavtsev, "Computation and flow visualization in high-speed aerodynamics," *Journal of Turbulence - J TURBULENCE*, vol. 6, 01 2005.

APPENDIX A

LOADING CONDITIONS

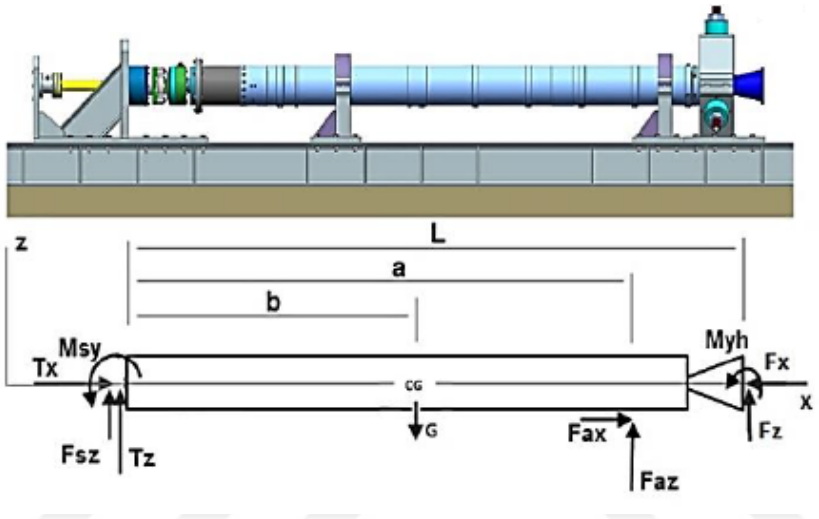

Figure A.1: Test Motor Free Body Diagram in Horizontal Axis (x-y plane)

The static equilibrium equations in the rocket motor x axis:

$$\sum F_x = 0; \qquad T_x + F_{ax} - F_x = 0$$

T_x : Axial thrust read from load sensor (force on horizontal (x) axis formed on support)

F_{ax} : Friction force between the rocket motor flange side to load sensor

F_x : Actual axial thrust

The static equilibrium equations in the horizontal axis:

$$\sum F_y = 0; \qquad T_y + F_{sy} + F_{ay} + F_y = 0$$

$$\sum M_z = 0; \qquad M_{sz} + aF_{ay} + LF_y + M_{zh} = 0 (M_{sz} = 0; M_{zh} = 0)$$

T_y : The force on the horizontal (y) axis on the support side

F_{ay} : Horizontal (y) axis component of the force generated by the nozzle side F_y : Horizontal (y) component of lateral thrust

F_{sy} : Horizontal force resulting from friction in the joint between the motor and the support

M_{sz} : The friction-induced moment in the joint between the rocket motor and the support

M_{zh} : Hinge Torque on Jet Vane

a : Distance between the point where the motor is connected to the support arm to the motor front side load sensor

b : Distance between motor front side load sensor and motor center of gravity

c : Distance between motor center of gravity and load cell located in motor nozzle side

d : Distance between jet nozzle side and load gauge

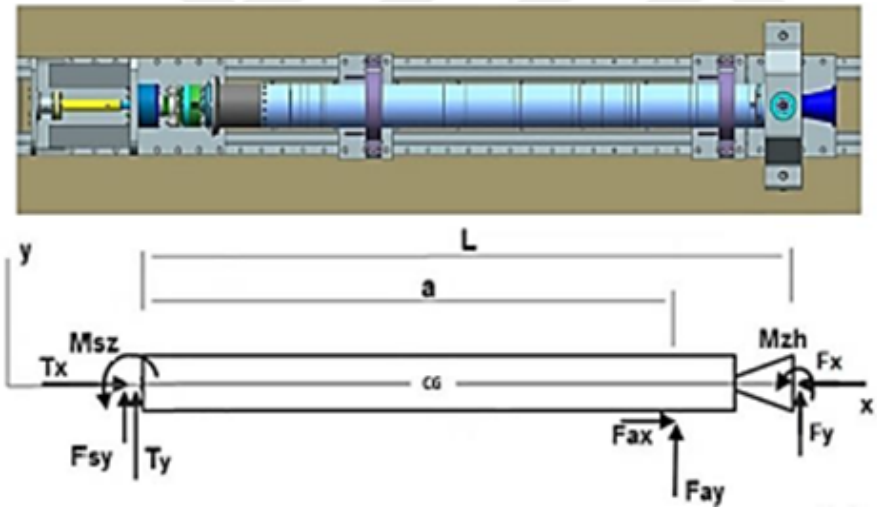

Figure A.2: Test Motor Free Body Diagram in Vertical Axis (z-x plane)

The static equilibrium equations in the vertical axis:

$$\sum F_z = 0; \quad T_z + F_{sz} + F_{az} - G + F_z = 0$$

$$\sum M_y = 0; \quad M_{sy} - (T_z - F_{sz})(a+b) - bF_{az} + cF_{bz} + (c+d)F_z + M_{yh} = 0$$

T_z : Force on the vertical (z) axis formed on the support side

F_{az} : Lateral thrust vertical (z) component on load cell which take place on rocket

motor nozzle side

F_z : Lateral thrust vertical (z) component

F_{sz} : The vertical force comes from the friction between the motor and the support joint

M_{sy} : Moment occurring from friction between the rocket motor and the support

M_{yh} : Hinge Torque on Jet Vane

The measured load cells and pressure data for each angle can be seen in Figure A.3, A.4 and A.5.

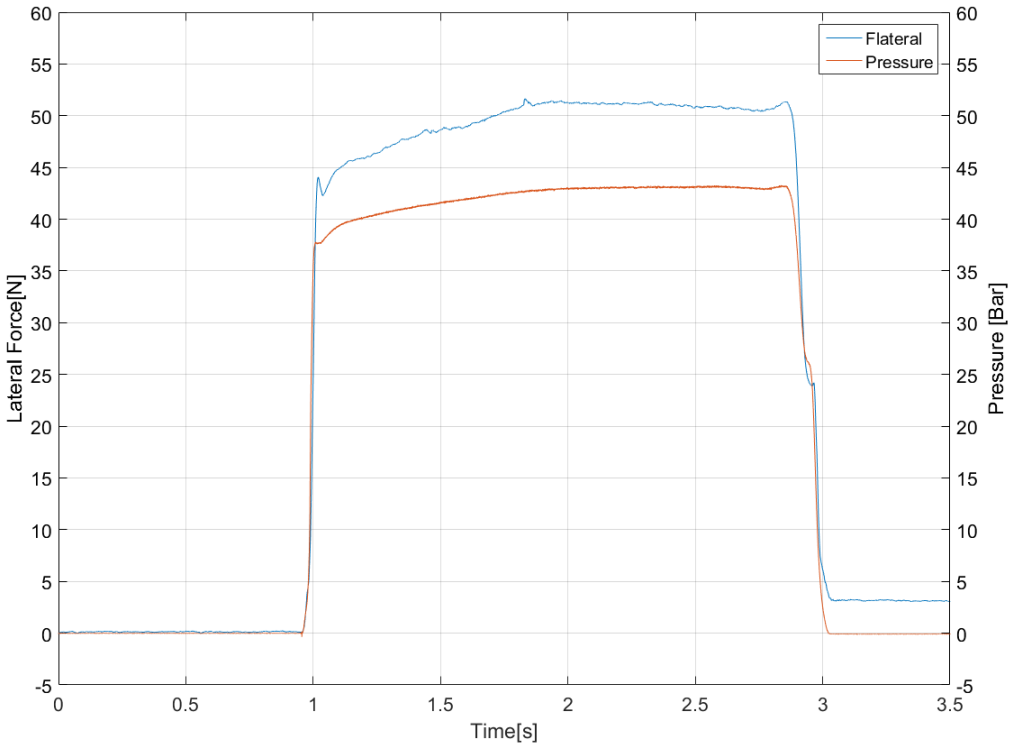

Figure A.3: Measured pressure and resultant force of 3 load cells data (F_2, F_3, F_4) [10°− case]

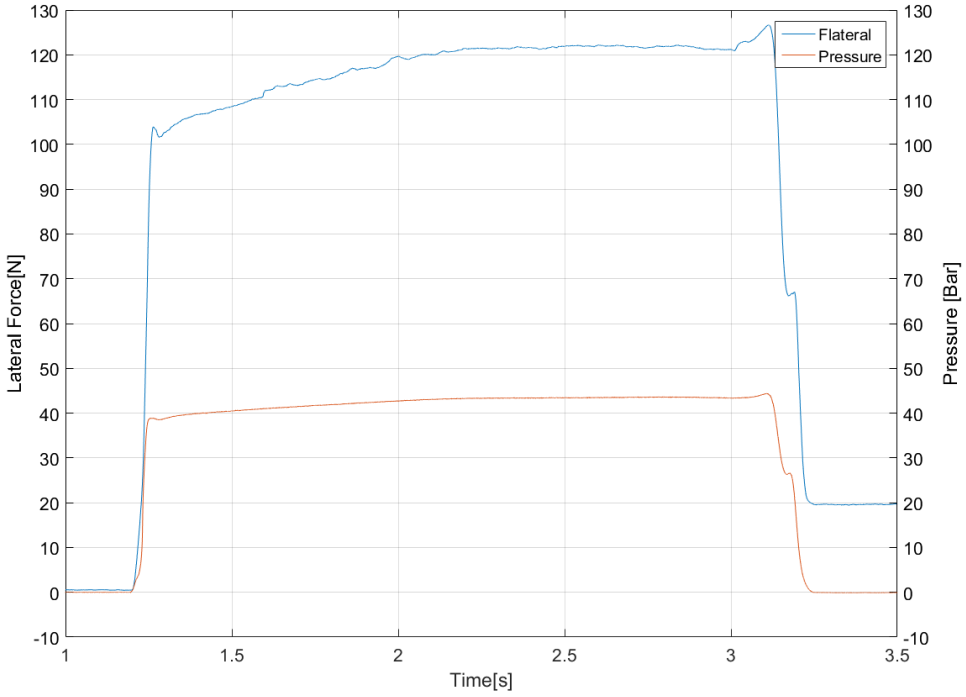

Figure A.4: Measured pressure and resultant force of 3 load cells data (F_2, F_3, F_4) [20°− case]

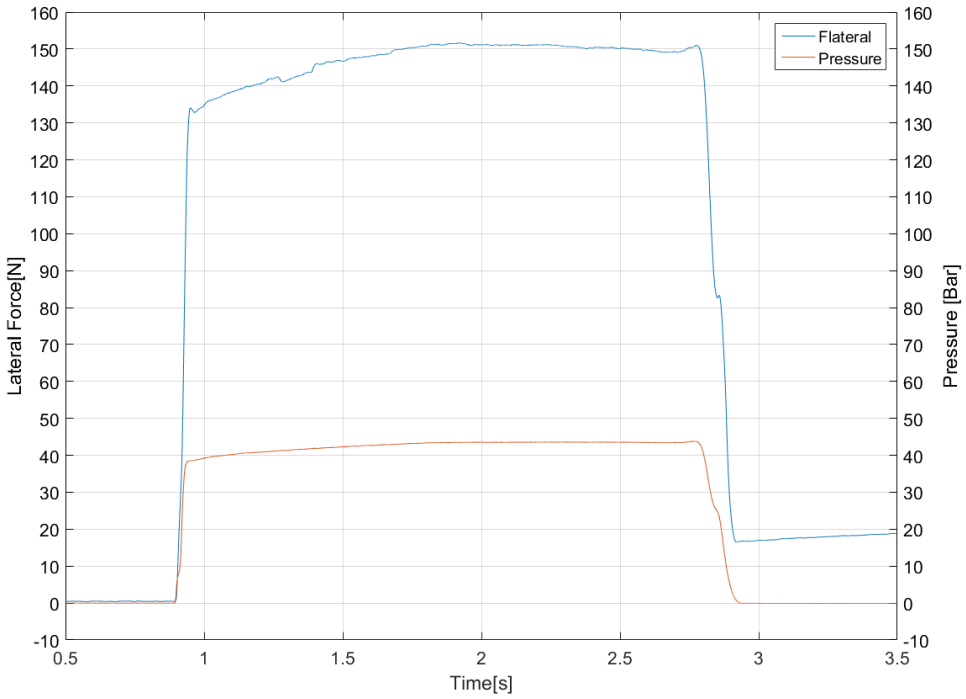

Figure A.5: Measured pressure and resultant force of 3 load cells data (F_2, F_3, F_4) [30°− case]